International Journal of Earth Sciences
https://doi.org/10.1007/s00531-020-01898-6

ORIGINAL PAPER

Timing and kinematics of flow in a transpressive dextral shear zone, Maures Massif (Southern France)

Matteo Simonetti[1] · Rodolfo Carosi[1] · Chiara Montomoli[1,2] · Michel Corsini[3] · Alessandro Petroccia[1] · John M. Cottle[4] · Salvatore Iaccarino[1]

Received: 28 February 2020 / Accepted: 22 June 2020

Abstract

The Maures–Tanneron Massif and the Corsica–Sardinia Block are two segments of the southern European Variscan belt that separated during the Late Oligocene–Miocene due to the opening of the Western Mediterranean basin. Correlation between the two regions, based mainly on petrologic similarities, is still debated. However, there are no detailed structural and petrochronological constraints on their potential relationships. In northern Sardinia there is well-documented evidence for a dextral transpressive shear zone that initiated after the first stage of frontal collision. In the Maures–Tanneron Massif, despite recognition of an important episode of transpressive deformation, it is still unclear which structures were active during this tectonic regime. We investigate in detail the kinematic of flow, finite strain and the timing of the deformation of the Cavalaire "Fault" (CF), a major ductile shear zone in the Maures–Tanneron Massif. In contrast to previous models, we argue that the CF is a transpressive shear zone characterized by a prevalent component of pure shear, while in-situ monazite geochronology reveals that the CF is initiated at ~ 323 Ma. The new data presented here, based on a multidisciplinary approach document, for the first time, the vorticity of the flow, finite strain and timing of this sector of the East Variscan Shear Zone, a regional-scale shear zone that characterized the Southern European Variscan belt during the late Carboniferous.

Keywords Maures–Tanneron massif · Transpression · East variscan shear zone · Sardinian basement · Vorticity · Monazite petrochronology

Introduction

The Variscan belt is the result of the Lower Carboniferous continent–continent collision between Laurentia–Baltica and Gondwana (Arthaud and Matte 1977; Burg and Matte 1978; Tollmann 1982; Matte 1986; Franke 1989). This continental collision likely involved

Electronic supplementary material The online version of this article (https://doi.org/10.1007/s00531-020-01898-6) contains supplementary material, which is available to authorized users.

✉ Rodolfo Carosi
rodolfo.carosi@unito.it

Matteo Simonetti
matteo.simonetti@unito.it

Chiara Montomoli
chiara.montomoli@unito.it

Michel Corsini
corsini@unice.fr

Alessandro Petroccia
alessandro.petroccia@edu.unito.it

John M. Cottle
cottle@geol.ucsb.edu

Salvatore Iaccarino
salvatore.iaccarino@unito.it

[1] Dipartimento Di Scienze Della Terra, Università Degli Studi Di Torino, via V. Caluso 35, 10125 Torino, Italy

[2] IGG-CNR PISA, via Moruzzi 1, Pisa, Italy

[3] Géoazur, Université Côte D'Azur, 250, rue A. Einstein, 06560 Valbonne, France

[4] Department of Earth Science, Lagoon Rd, Santa Barbara, CA 93106, USA

Published online: 07 July 2020

also small microplates, such as Avalonia and Armorica, drifted away from Gondwana during the early Palaeozoic and subsequently collided against Baltica and Laurentia (Scotese and McKerrow 1990; Matte 2001; Stampfli and Borel 2002; Franke et al. 2017 and references therein). Remnants of such terranes crops out in Corsica (Rossi et al. 1993, 2009), where they are sealed together with the internal Variscan zone by Visean Mg–K granites, and in the Alps (Ballèvre et al. 2018). The Variscides, the portion of the belt exposed in Central and Western Europe, are traditionally regarded as key areas for understanding the evolution of this orogen (Franke 1989; Oncken et al. 1999; Carosi and Palmeri 2002; Corsini and Rolland 2009) where a composite orocline is recognized. This composite orocline consists in two main branches: the western Ibero–Armorican arc (Matte 1986; Dias and Ribeiro 1995; Dias et al. 2016; Fernández-Lozano et al. 2016) and the eastern branch delimited, to the east, by a regional-scale shear zone, known as East Variscan Shear Zone (EVSZ; Matte 2001, Corsini and Rolland 2009; Carosi et al. 2012, 2016; Padovano et al. 2011, 2014; Simonetti et al. 2018, 2020).

Reworking and fragmentation of the southeastern portion of the belt during the Alpine cycle makes it difficult to correlate Variscan fragments in the Mediterranean area. The Maures–Tanneron Massif (MTM, Fig. 1a) is located in a key position because it is in between the overprinted sector of the Variscan belt (Alpine External Crystalline Massifs) and a still preserved fragment (Corsica–Sardinia Block) largely escaped from the Alpine overprinting.

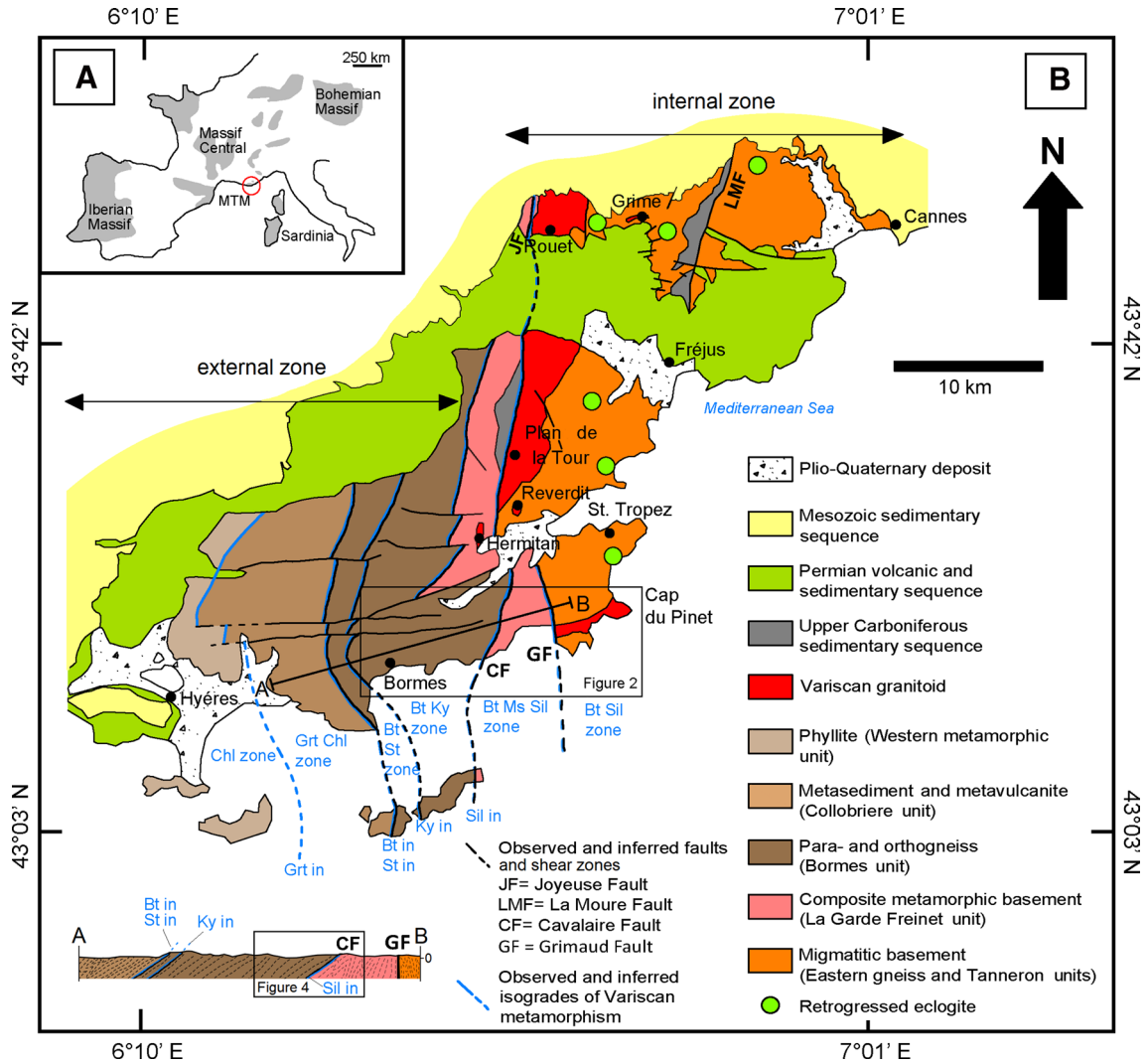

Fig. 1 **a** Distribution of the Variscan basement in Europe and location of the Maures–Tanneron Massif (MTM, red circle); **b** Simplified sketch map of the Variscan basement of the Maures–Tanneron Massif showing the main units and tectonic contacts, metamorphic zonation is reported (modified after Buscail 2000; Bellot 2005; Compagnoni et al. 2010; Schneider et al. 2014; Oliot et al. 2015; Gerbault et al. 2018). Detail of the study area is reported in Fig. 3

The correlation between the MTM and Sardinia is supported by lithological similarities (Ricci and Sabatini 1978; Elter and Pandeli 2005; Corsini and Rolland 2009; Rossi et al. 2009; Schneider et al. 2014; Gerbault et al. 2018) and paleomagnetic data (Edel 2000; Advokaat et al. 2014; Edel et al. 2018). Other authors, proposed that the Corsica–Sardinia Block was closely connected to Iberia (Stampfli et al. 2002; Kirscher et al. 2011; Turco et al. 2012; von Raumer et al. 2013; Dilek and Furner 2019), whereas others proposed different paleogeographic reconstructions (see Guerrera et al. 2019).

Some authors (Rollet et al. 2002; Rosenbaum et al. 2002; Advokaat et al. 2014; van Hinsbergen et al. 2020) suggested that the MTM separated from Corsica–Sardinia Block during the Late Oligocene–Miocene due to the opening of the Western Mediterranean back-arc basin.

Correlation between the MTM and the Corsica–Sardinia Block is also complicated since different dataset regarding the Variscan tectonics, particularly concerning the transpressive stage, are present. In northern Sardinia the presence of a late-Variscan transpressive shear zone (the Posada–Asinara Line), located between the high-grade and the medium-grade metamorphic complexes, is well-documented (Carosi and Oggiano 2002; Carosi and Palmeri 2002). In this area kinematics, flow regime and timing constraints of the transpressive structures are available (Carosi et al. 2012 and references therein; Cruciani et al. 2015; Di Vincenzo et al. 2004). On the contrary, in the MTM, despite an important episode of transpressive deformation being recognized (Bellot and Bronner 2000; Bellot et al. 2002; Bellot 2005; Corsini and Rolland 2009; Rolland et al. 2009; Schneider et al. 2014), it is not clear which structures (and related timings) were active during the transpressive regime.

Vauchez and Bufalo (1985, 1988), Morillon et al. (2000) and Rolland et al. (2009) described the Joyeuse-Grimaud Faut and the Lamoure Fault (Fig. 1b) as the main structures associated with transpressional regime in the MTM. Alternatively, Schneider et al. (2014) described the Cavalaire Fault (CF, Fig. 1b) as the main shear zone active during transpression.

We present the results of structural and microstructural analyses of key areas in the MTM combined, for the first time, with an analysis of the kinematics of the flow, finite strain and in-situ petrochronology of mylonites within the Cavalaire Fault. The main aim of this contribution is to clarify which structures were active during transpressive tectonics, their timing and the possible correlation with other segments of the EVSZ. The presented data carry a contribution for understanding the deformational history of the MTM and enhancing its potential correlations with the northern Sardinia.

Geological setting of the Maures–Tanneron Massif

The MTM (Fig. 1a) is the southernmost segment of the Variscan belt in France (Chabrier and Mascle 1975; Matte 2001). The MTM is composed of low- to high-grade metamorphic rocks, the latter intruded by Carboniferous granitoids (Crevola and Pupin 1994). The Maures Massif is separated from the Tanneron Massif by the E-W trending Permian Esterel basin (Fig. 1b). The western domain of the MTM records Barrovian metamorphism increasing in grade from west to east (Buscail 2000; Bellot 2005; Corsini and Rolland 2009; Schneider et al. 2014; Oliot et al. 2015). Several Variscan metamorphic units are distinguished (review in Schneider et al. 2014; Fig. 1b). From W to E, the main units are: (1) the western metamorphic unit (Fig. 1b) made by Early Paleozoic low-grade phyllite belonging to the chlorite zone; (2) the Collobrières unit (Fig. 1b), included within the garnet-chlorite zone, consisting of iron-rich metasediments (quartzite, marble and gneiss) and metavolcanic rocks of the alkaline leptyno-amphibolitic complex (Bard and Caruba 1981). The latter is interpreted as a volcano-sedimentary suite emplaced during Cambrian continental rifting (Briand et al. 2002; Innocent et al. 2003); (3) the Bormes unit (Fig. 1b), made up of the Bormes orthogneiss and associated metasediments, affected by Barrovian metamorphism from the biotite-staurolite zone up to the biotite-kyanite zone; (4) the La Garde-Freinet unit (Fig. 1b) containing micaschist, migmatitic paragneiss and orthogneiss with acid, mafic and ultramafic lenses represented by an association of amphibolite and leptynite. Barrovian metamorphism is in the sillimanite-biotite zone; (5) the Eastern Gneiss and Tanneron units (Fig. 1b), affected by metamorphism in the sillimanite–biotite zone, are made of migmatitic ortho- and paragneiss with associated mafic eclogite lenses showing a polyphase metamorphism. The La Garde-Freinet and Eastern Gneiss units are intruded by syn-kinematic calc-alkaline and peraluminous granitoids (Fig. 1b): the Hermitan granite (in the La Garde-Freinet unit) and the Plan-de-la-Tour granite (in the Eastern Gneiss unit), the last one cropping out in the core of a regional-scale N-S trending antiform (Rolland et al. 2009). La Garde-Freinet, Eastern Gneiss and Tanneron units are part of the internal zone (Fig. 1b) characterized by widespread partial melting and syn-tectonic granitic intrusions (Schneider et al. 2014). Relicts of high-pressure in mafic rocks also occur in the internal zone. Collobrières and Bormes units are part of the external zone (Fig. 1b) characterized by a low-grade metamorphism and by the lack of high-pressure mafic relicts. The subdivision of the Maures Massif in

two different tectonic-metamorphic zones, internal and external zones, was pointed out by Vauchez and Bufalo (1985, 1988) and Morillon et al. (2000) who described the presence of a high-temperature transcurrent shear zone, the Joyeuse–Grimaud Fault (Fig. 1b), between the two zones. Recently, Schneider et al. (2014) recognized that the internal and external zones are separated by the CF (Fig. 1b), interpreted as a major polyphase shear zone, rather than by the Joyeuse–Grimaud Fault located in the internal zone.

The CF was initially studied by Bellot et al. (2000, 2002). These Authors recognized a first top-to-the-E-SE thrust-related kinematic during Early Carboniferous, followed by a reactivation as a normal fault during late-Variscan phase, related to extensional tectonics, allowing a progressive thinning of a previously thickened crust. Recent studies (Schneider et al. 2014; Oliot et al. 2015; Gerbault et al. 2018) are in agreement with the first top-to-the-E-SE thrust-sense movement, but recognized a later reactivation in a transpressional regime associated to the exhumation of the mid- and lower crust between ~ 330 and 310 Ma.

In the MTM, Schneider et al. (2014) recognized several tectono-metamorphic stages. In the internal zone, relicts of eclogite-facies metamorphism (M_0) preserved in metabasic lenses, are related to an early stage of Siluro–Devonian subduction. A collisional stage, mostly preserved in the external zone, is marked by nappes stacking with top-to-the-west tectonic transport (D_1), followed by backthrusting of the nappes towards the east (D_2). In the internal zone, exhumation of the tectonic units occurred in a context of transpressive regime (D_3). Nappes stacking and backthrusting were associated with typical Barrovian-type metamorphism M_1, progressively followed by LP-HT metamorphic stages, M_2 and M_3, during Carboniferous.

Methods for structural analysis

We focused on two key areas of the Maures–Tanneron Massif (Fig. 2) where the contact between internal and external zones is marked by a well-exposed high-strain zone, the CF. We performed mesostructural analysis combined with microstructural study on field-oriented samples (Figs. 2, 3) collected within the Bormes and La Garde-Freinet units. The structural maps of the studied sector within the high-strain zone and the position of the collected samples are reported in Fig. 3.

Samples were cut perpendicular to the main foliation and parallel to the mineral lineation (XZ section of the finite strain ellipsoid with X > Y > Z). The software EllipseFit (Vollmer 2015) was used to obtain parameters needed for vorticity and for finite strain calculations. Kinematics of the flow, i.e. components of pure and simple shear acting simultaneously during deformation (Xypolias 2010 for a review) in the high-strain zone, were estimated using two independent kinematic vorticity gauges: the C' shear band

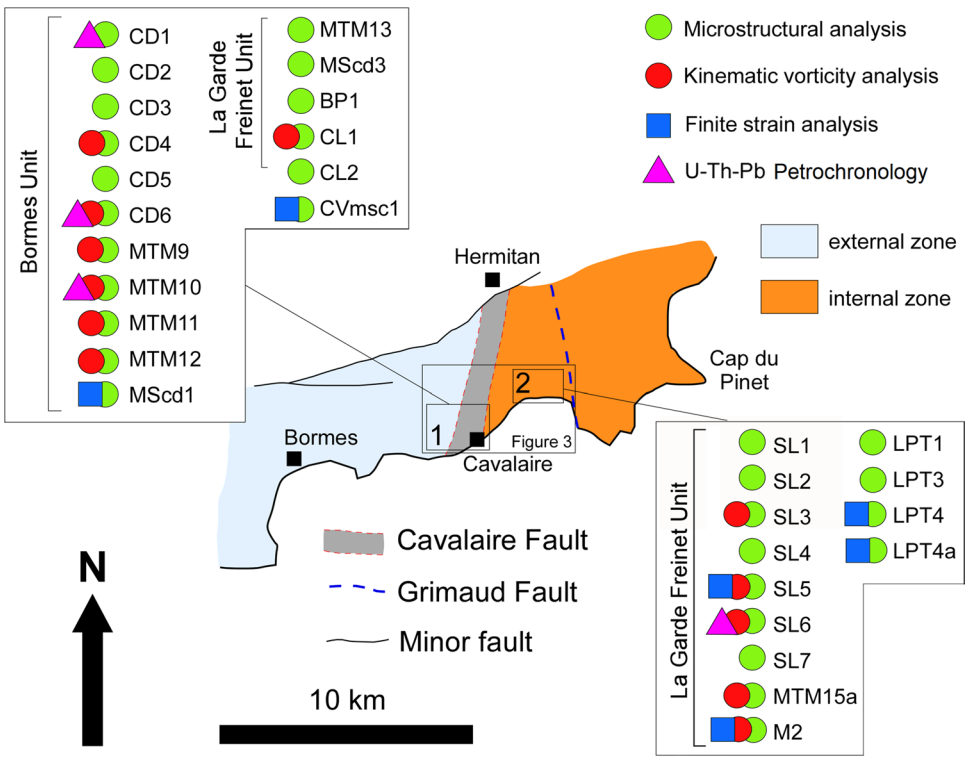

Fig. 2 Sketch with sampling locations (1 and 2) in the Maures Massif. The samples location and the corresponding type of analysis are shown. Details of the selected study areas are given in Fig. 3

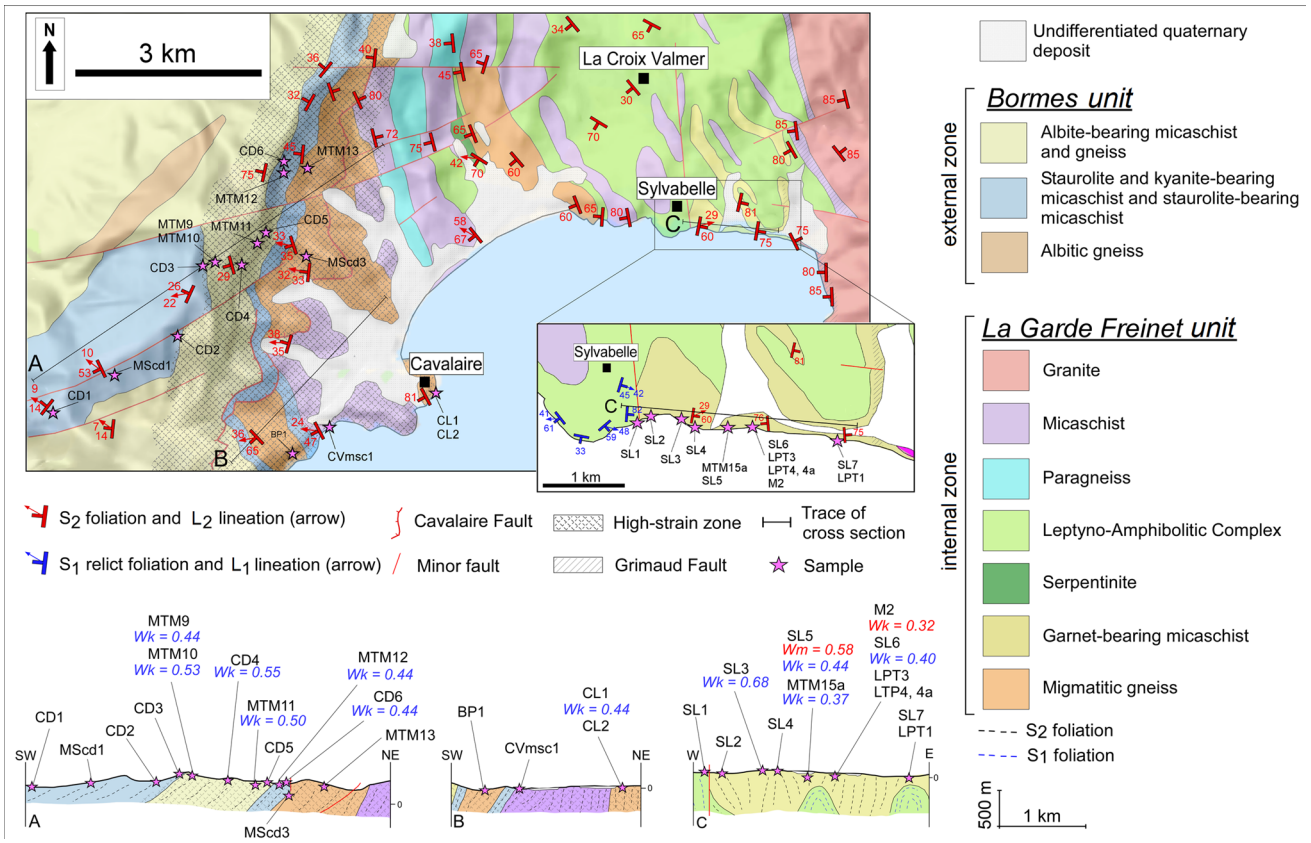

Fig. 3 Geological sketch maps of the study areas (location is reported in Fig. 2) with samples locations (modified from geological map of Saint Tropez-Cap Lardier 1/50,000, editions BRGM; the limits of the high-strain zone of the Cavalaire Fault are modified after Bellot et al. (2002)). Geological cross sections with samples position and the relative vorticity number are also reported

method (Kurz and Northrup 2008; Gillam et al. 2013) and the stable porphyroclasts method (Passchier 1987; Wallis et al. 1993). The latter technique was restricted to only two suitable samples of garnet-bearing micaschist containing an adequate number of porphyroclasts.

In a flow regime two flow apophyses are recognized, separating different domains of particle paths (Fossen 2016). The kinematic vorticity number (Wk) is defined as the cosine of the angle between the two apophyses (Fossen 2016). In the case of pure shear (i.e. with two orthogonal flow apophyses) Wk is 0, whereas Wk is 1 in the case of simple shear (flow apophyses are coincident). Simple and pure shear equally contribute to flow at a value of Wk = 0.71 (Law et al. 2004). Vorticity is nearly independent of volume loss (Fossen and Cavalcante 2017). Indeed, in most of the shear zones developed in both magmatic and metamorphic rocks (excluding slates and phyllites) compaction is limited and the uncertainties related to volume loss are small with respect to the intrinsic error associated with a specific vorticity gouge (Fossen and Cavalcante 2017).

The first applied method (Kurz and Northrup 2008; Gillam et al. 2013) is based on the measurement of the orientation of C' planes with respect to the shear zone boundaries. C' planes nucleated as the bisector of the angle (ν) between the two flow apophyses. The component of simple shear is inversely proportional to the amplitude of this angle (Platt and Vissers 1980; Simpson and De Paor 1993; Kurz and Northrup 2008). We derive the kinematic vorticity with the relation $Wk = \cos 2\nu$ (Kurz and Northrup 2008). Some variations in the ν angles exist because during progressive deformation C' planes tend to be passively rotated towards the fabric attractor apophysis (A2). For this reason we select the maximum value of ν for the calculation since this is regarded as the closest approximation of the initial nucleation angle of C' plane (Kurz and Northrup 2008).

The second applied vorticity gauge consists in measuring the axial ratio of porphyroclasts (R) and the angles between their major axis with respect to the mylonitic foliation (Passchier 1987; Wallis et al. 1993). These data are plotted on a graph to estimate a critical axial ratio, Rc (Wallis et al. 1993), which discriminates the field where porphyroclasts reach a stable position from a field where they continue to rotate. To minimize the uncertainties, two Rc values

have been chosen (Rc minimum and Rc maximum) and an average vorticity has been calculated using the relation $Wm = (Rc^2 - 1)/(Rc^2 + 1)$. The stable porphyroclasts method is based on three main assumptions (Jeffery 1922; Iacopini et al. 2011 and references therein): (1) porphyroclasts behave as rigid objects floating in a Newtonian viscous matrix at constant deformation; (2) there is no interaction and slip between clasts and matrix; (3) there is no interference between the particles. The first condition has been assessed by verifying that the porphyroclasts do not show internal deformation and they are harder to deform compared to the matrix (Iacopini et al. 2011). The second condition was tested by plotting porphyroclast distribution against theoretical curves of Mulchrone (2007a, b), as suggested by Iacopini et al. (2011). The third condition is satisfied if the porphyroclasts are sufficiently distant from one other to freely rotate. To avoid mutual interference the distance between porphyroclasts should be larger than their maximum long axis (Ildefonse et al. 1992). The quoted uncertainty on vorticity estimates is ± 0.1 (Tikoff and Fossen 1995). According to Iacopini et al. (2011) the propagation of systematic errors indicates that for medium to low vorticity numbers ($Wm < 0.8$), vorticity data are strongly biased and more realistic systematic uncertainty is ± 0.2.

To distinguish between transpression and transtension (Fossen and Tikoff 1993; Fossen et al. 1994) we calculated the angle θ between the maximum ISA in the horizontal plane and the shear zone boundary. The calculation was performed using the formula $\theta = (\arcsin Wk)/2$ (Xypolias 2010).

Geometry of the finite strain ellipsoid is the result of the interaction between the simple shear and the coaxial component of deformation. Finite strain and kinematic vorticity are therefore linked and can be used to distinguish between different types of deformation (Fossen and Tikoff 1998).

Finite strain analysis, using the center-to-center method (Fry 1979), was performed on six samples (M2, SL5, Lpt4, Lpt4a, MScd1, CVmsc1; Fig. 2) collected across the high-strain zone. We used garnet porphyroclasts, with similar grain size, as strain markers in four samples belonging to the garnet-bearing micaschist of the La Garde-Freinet unit and in two samples of sheared staurolite-garnet-bearing micaschist of the Bormes unit (Figs. 1, 2, 3). Samples were cut and polished perpendicular to the foliation and both parallel and perpendicular to the mineral lineation to visualize both the XZ and the YZ sections of finite strain ellipsoid. The center-to-center method is based on the redistribution of the centers of the strain markers caused by deformation, having an original homogeneous distribution in the undeformed state (see Genier and Epard 2007 for a critical review). The Fry method is independent of the shape of the strain markers since the result is only a function of the distribution and the mutual distance of the objects centers. The analysis consists in the choice of a reference point that is moved on the centers of the markers to project the nearest centers to the analyzed marker center. Repeating this procedure a dozen times, a blank area (or an area with low density of points) representative of the finite strain ellipse and surrounded by an area with higher density of points, appears. Strain and vorticity pairs from the same sample were combined to calculate the percentage of shortening and stretching perpendicular and parallel to the mylonitic fabric, respectively (Wallis et al. 1993; Law et al. 2004; Law 2010).

Structural analysis

The CF, as testified by field observations, is characterized by a NE-SW trending km-thick high-strain zone, involving biotite-kyanite and biotite-muscovite-sillimanite zones (Figs. 1, 3). West of the CF unsheared gneiss and micaschist of the Bormes unit (external zone) are present, whereas migmatite of the La Garde-Freinet unit (internal zone) crops out on the eastern side of the CF (Fig. 4). In the field, a deformation gradient is recognized toward the core of the CF high-strain zone (Fig. 4). From west to east, within the high-strain zone, staurolite-kyanite-bearing micaschist and staurolite-bearing micaschist, belonging to the Bormes unit, have been mapped. They show a biotite + white mica continuous foliation, dipping to the NW, with a mineral lineation, defined by staurolite (Fig. 5a), trending NW–SE and plunging to the NW. Shear planes dip toward W-NW at variable angle between 14° and 53°.

Asymmetric strain fringes around staurolite porphyroclasts (Fig. 6a) and C-S fabric indicate a top-to-the-NW normal sense of shear. Boudins of quartz and feldspar rich-material, observed on both the XZ and YZ sections of the finite strain ellipsoid (Fig. 6b), are often present. Folded boudins also occur (Fig. 6c). The main foliation is deformed by a steeply dipping crenulation cleavage that is occasionally associated to the dynamic recrystallization of chlorite (Fig. 6d). Micaschist is in contact with the mylonitic gneiss and mylonitic micaschist of the CF and shows a penetrative mylonitic foliation steeply dipping to the W, and a mineral lineation plunging to the W-NW (Fig. 5b). The sense of shear, highlighted by S-C and S-C' fabric, is top-to-the-NW. In some sectors a sub-vertical crenulation cleavage, deforming the mylonitic foliation, is present. La Garde-Freinet unit, to the east of the mylonitic gneiss of the CF (Figs. 1, 3), is affected by non-coaxial deformation and folds. Sheared migmatite shows a sub-vertical foliation defined by biotite and sillimanite (Fig. 5c). Both dextral and sinistral kinematic indicators occur in these rocks (Fig. 6e). F_2 folds, confined within the high-strain zone, have been recognized in migmatite, amphibolite and garnet-bearing micaschist. F_2 folds

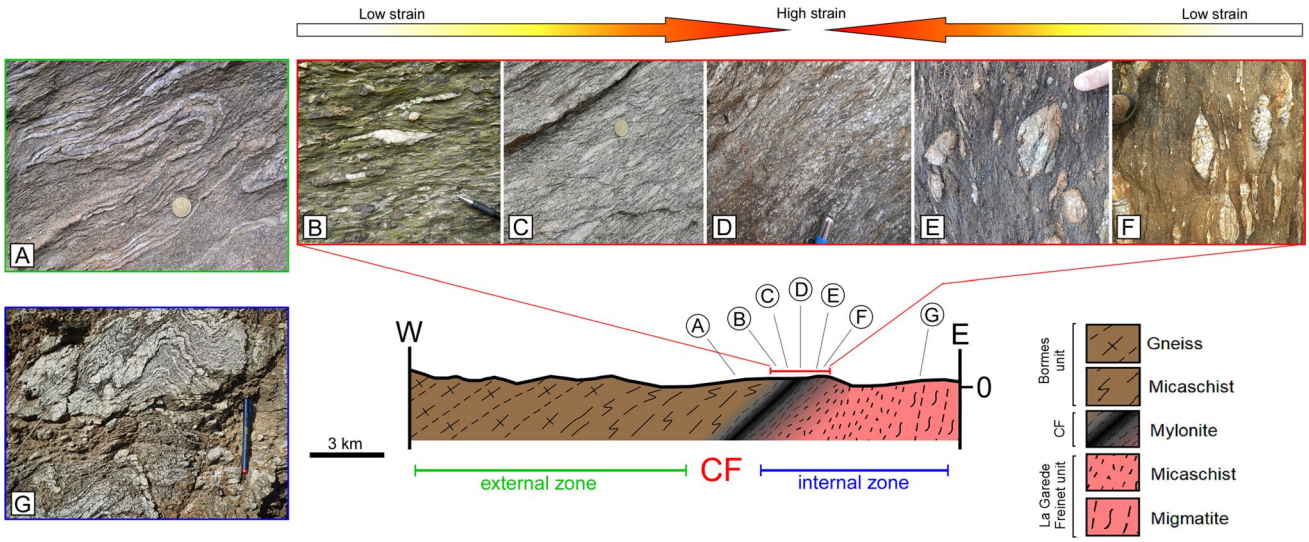

Fig. 4 Schematic cross-section across the contact between internal and external zones (location is reported in Fig. 1) summarizing the main field-observed deformational features of the different structural domains. **a** folded micaschist of the external zone (Bormes unit) cropping out to the W of the CF; **b** mylonite of the western side of the CF, developed at the expense of staurolite-bearing micaschist (Bormes unit); **c** mylonite at the expense of paragneiss; **d** mylonitic paragneiss in the core of the CF; **e** mylonite at the expense of migmatite in the internal zone (La Garde-Freinet unit); **f** mylonite of the eastern limb of the CF affecting migmatite of the internal zone (La Garde-Freinet unit); **g** folded migmatite of the internal zone (La Garde-Freinet unit; same outcrop described in Schneider et al. (2014))

have sub-vertical axes and axial planes (Fig. 5d) parallel to the main foliation (Fig. 6f). Steeply dipping mineral lineations, L_2, have been observed on the main foliation (Fig. 5d). An older S_1 foliation is preserved in the hinge zones of the folded amphibolite. This foliation is parallel to the S_2 foliation of the micaschist in the limbs of the F_2 folds (Fig. 6g). Later open folds F_3, with axes and axial planes dipping at low-angle to the SW, causes a variation in the dip angle and the dip direction of the mylonitic foliation (Fig. 6h). A sub-vertical W-NW-ESE S_4 crenulation cleavage occurs sporadically (Fig. 5e), A_4 microfold axis plunges toward W-NW (Fig. 5e) and an intersection lineation, between S_4 and S_2, plunges toward the NW (Fig. 4e). Brittle and brittle-ductile shear planes affect the mylonitic foliation, striking NNE-SSW with variable dip (Fig. 5f) and a top-to-the-W-NW sense of shear.

Microstructures of the high-strain zone

Microstructural analysis was performed on sheared samples of the CF (Figs. 2, 3). Foliations and kinematic indicators have been classified according to Passchier and Trouw (2005). Quartz microstructures, indicative of dynamic recrystallization, are defined according to Piazolo and Passchier (2002), Stipp et al. (2002) and Passchier and Trouw (2005).

Sheared staurolite-bearing micaschist, belonging to the Bormes unit, and involved in the CF, are characterized by a continuous foliation made of biotite + white mica. The foliation wraps around kyanite, staurolite and garnet porphyroclasts showing an internal foliation, mainly composed of elongate quartz. The internal foliation in the porphyroclasts is generally not continuous with the external foliation (Fig. 7a), however in some staurolite crystals, an internal foliation at the grain rims is concordant with the external foliation (Fig. 7b). These observations support the interpretation that staurolite growth predates, and is locally synchronous, with the development of the mylonitic foliation. A top-to-the-NW normal sense of shear is highlighted by the presence of asymmetric strain fringes around porphyroclasts of staurolite and garnet. Quartz lobate and ameboid grain boundaries suggest dynamic recrystallization by grain boundary migration (Fig. 7c). The CF is associated with a mylonitic foliation overprinting previous structures developed in micaschist and gneiss of the Bormes unit (external zone) and in migmatite, amphibolite and micaschist of the La Garde-Freinet unit (internal zone). In the micaschist and gneiss of the Bormes unit, the mylonitic foliation is defined by biotite, white mica, ± fibrolitic sillimanite. Quartz shows lobate grain boundaries suggesting a dynamic recrystallization by grain boundary migration. However, in some sectors, incipient subgrain rotation recrystallization is recognized. K-feldspar sometimes shows mechanical twinning and undulose extinction and locally minor fractures at high-angle to

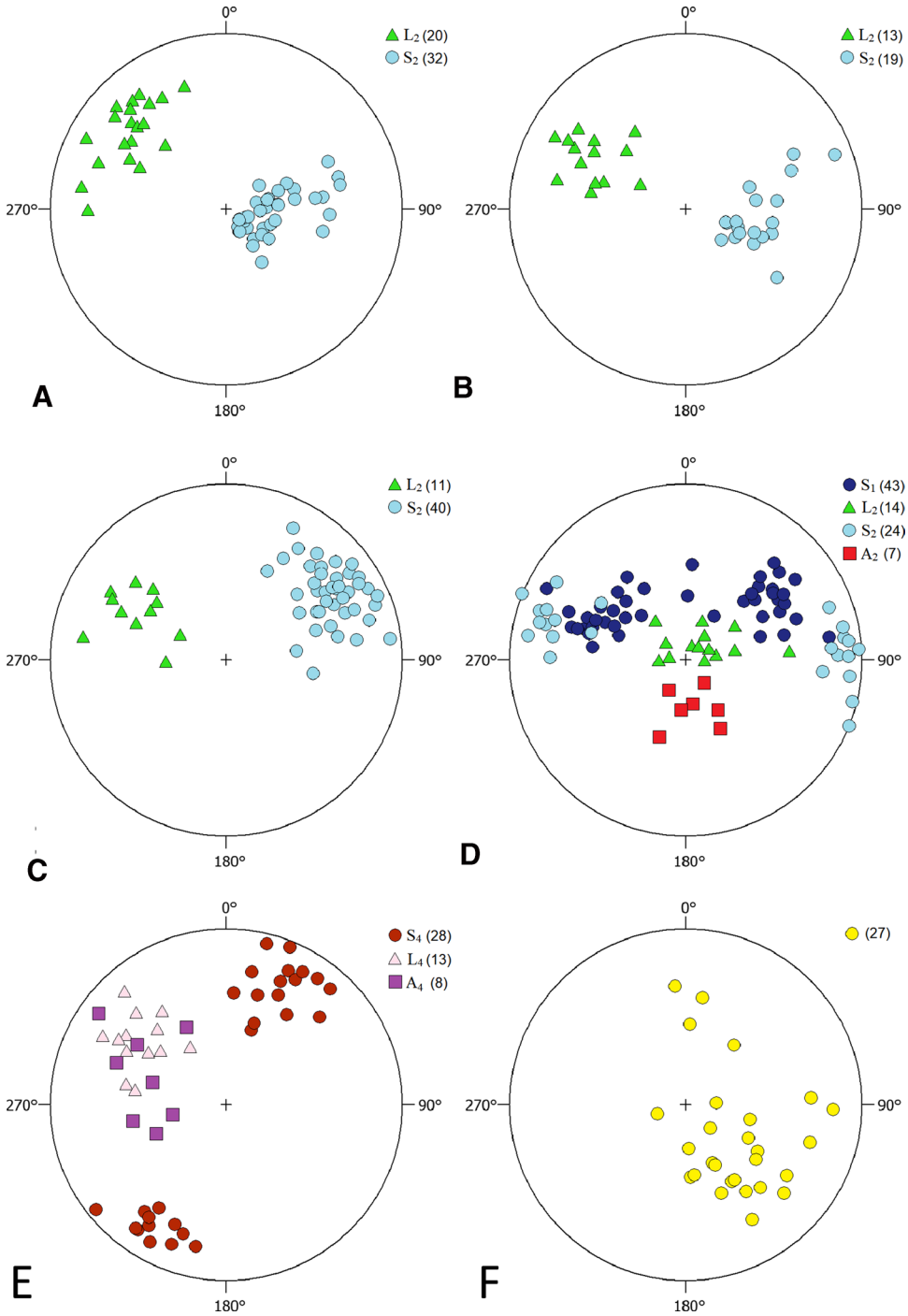

Fig. 5 Equal angle projection (lower hemisphere) of main structural elements: **a** poles to S_2 foliation planes (dots, 32 data) and L_2 stretching lineation (triangles, 20 data) in the staurolite-bearing micaschist of the kyanite-biotite zone adjacent to the CF; **b** poles to S_2 foliation planes (dots, 19 data) and stretching lineation L_2 (triangles, 13 data) in the mylonitic gneiss of the CF; **c** poles to S_2 foliation planes (dots, 40 data) and L_2 stretching lineation (triangles, 11 data) in sheared migmatite of the Cavalaire Fault; **d** structural elements of mylonite of the La Garde-Freinet unit east of the Cavalaire Fault. Poles to S_1 foliation planes in the amphibolite (dark dots, 43 data), poles to S_2 foliation planes in the garnet-bearing micaschist (light dots, 24 data) and L_2 stretching lineation (triangles, 14 data), A_2 fold axis (square, 7 data); **e** structural elements associated to the crenulation cleavage measured in all the lithotype of the contact zone. L_4 intersection lineation between the main foliation (S_2) and crenulation cleavage (S_4) planes (triangles, 13 data), poles to S_4 crenulation cleavage (dots, 28 data), A_4 fold axis of crenulation microfolds (square, 8 data); **f** poles to brittle and brittle-ductile shear planes measured across the high-strain zone (dots, 27 data)

the mylonitic foliation. S-C and S-C' fabrics indicate a top-to-the-NW normal sense of shear (Fig. 7d). In the migmatite (La Garde-Freinet unit, internal zone), the mylonitic continuous foliation is defined by biotite and sillimanite. The mylonitic foliation wraps around sheared leucosomes consisting of quartz and feldspars. Folded amphibolite layers are composed of plagioclase and green amphibole-rich levels alternating with quartz + plagioclase and garnet bands. Garnet-bearing micaschist, occuring around amphibolite, shows a spaced schistosity with sharp and parallel cleavage domains defined by biotite + white mica. Garnet porphyroclasts show an internal foliation, marked by inclusions of elongated quartz, oriented at a high-angle with respect to the external foliation (Fig. 7e). Quartz shows lobate grain boundaries. Rotated porphyroclasts, S-C and S-C' fabric, point to a top-to-the-NW sense of shear (Fig. 7f).

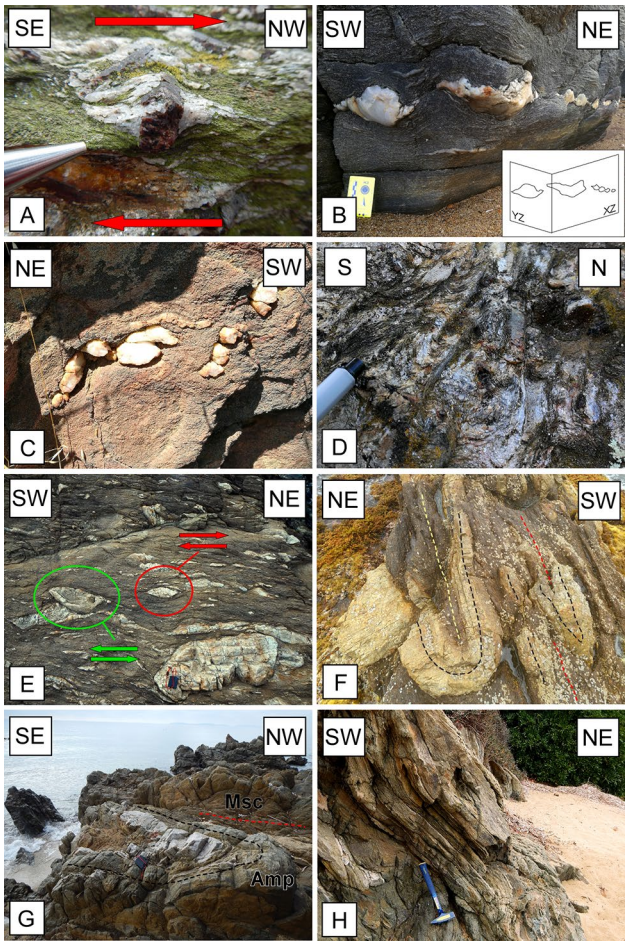

Fig. 6 **a** Asymmetric quartz strain fringes around a staurolite porphyroclast in staurolite-bearing micaschist showing a top-to-the-NW sense of shear; **b** boudins developed at the expense of quartz and feldspar rich levels recognizable both on the XZ and YZ section of the finite strain ellipsoid; **c** folded boudins in sheared rocks of the Cavalaire Fault; **d** steeply dipping S_4 cleavage defined by chlorite and deforming S_2 foliation in the staurolite-bearing micaschist (plan view); **e** sheared migmatite showing both dextral and sinistral sense of shear; **f** examples of F_2 syn-shear folds deforming quartz-rich domain in the garnet-bearing micaschist (black dashed line) with sub-vertical both axis and axial plane (yellow dashed line), parallel to the main S_2 foliation (red dashed line); **g** syn-shear fold (F_2) deforming an older relict S_1 foliation (black dashed line) in the amphibolite (Amp). S_1 is preserved in the hinge zones of the fold, whereas it parallelized to the S_2 foliation of the garnet-bearing micaschist (Msc) in the limbs (red dashed line). Foliation in the micaschist and F_2 axial plane are parallel; **h** late F_3 open folds with sub-horizontal axes and low-angle axial planes deforming the S_2 foliation in garnet-bearing micaschist

Kinematic vorticity and finite strain analysis

Results of the kinematic vorticity analysis with C' shear band and stable porphyroclast-methods are reported in Tables 1 and 2, respectively. Examples of polar histograms (for sample MTM12 and SL5), used to derive the angle ν, are provided in Fig. 8, whereas the full dataset is given in online resource 1. For the stable porphyroclasts method, preliminary Mulchrone tests are shown in Fig. 9a and b, whereas the porphyroclasts distributions are given in Fig. 9c and d. The twelve samples (see Fig. 3 for sample location) analyzed by the C' shear band method give a vorticity number ranging from 0.40 to 0.68, with a mean of 0.47 and a mode of 0.44. These values indicate a flow regime characterized by an important contribution of pure shear, ranging between 52 and 66% (Fig. 10a).

In sample M2 we detected, through the stable porphyroclast method, a minimum Rc of 1.38 and a maximum Rc of 1.42 corresponding to Wk values of 0.31 and 0.34, respectively. In sample SL5 minimum and maximum Rc values are 1.73 and 2.2 corresponding to Wk between 0.50 and 0.66. These values indicate a 55–75% pure shear, in good agreement with the results based on C' shear band vorticity gauge.

Data obtained with the stable porphyroclast method are regarded as reliable since all the main assumptions (see above) of the method are satisfied. Indeed: garnet and feldspar porphyroclasts do not show significant internal deformation and are harder to deform compared to the mica-rich matrix; from the compiled Mulchrone diagrams (Fig. 9) our data do not fit the theoretical curve calculated for a system in which slip between porphyroclasts and matrix occurs; the selected garnets and feldspars are free to rotate in the matrix without mutual interference because the distance between porphyroclasts (~2 mm as average) is larger than their maximum long axis (~1.2 mm as average size).

According to the calculated θ angle, all samples plot in the field of pure shear-dominated transpression (Fig. 10b).

The complete finite strain dataset, obtained by the center-to-center method, is reported in online resource 2, whereas selected examples (sample M2, SL5 and MScd1) are reported in Fig. 11a. Finite strain analysis indicates an axial ratio of 2.14, 2.56, 2.11, 2.23, 2.18 and 1.79 on the XZ sections and 1.47, 1.72, 1.66, 1.49, 1.44 and 1.77 on YZ sections of the finite strain ellipsoid for sample M2, SL5, CVmsc1, Lpt4a, MScd1 and Lpt4, respectively. The value of the shape parameter of the strain ellipsoid (K) is 0.95 for sample M2, 0.68 for sample SL5, 0.39 for sample CVmsc1, 1 for sample Lpt4a, 1 for sample MScd1 and 0.01 for sample Lpt4. In the Flinn diagram (Flinn 1962), most of the samples fall in the general flattening field, whereas samples M2, Lpt4a and MScd1 are close to plane strain condition (Fig. 11b).

Combining Wk values and finite strain estimates from the same sample, following Wallis et al. (1993) and Law et al. (2004), we calculate 30% and 36% shortening in sample M2 and SL5, respectively. This relation provides reliable stretching values only in the case of plane strain where, for a given amount of shortening, all of the elongation is transport-parallel and accommodated along the *X* axis of the

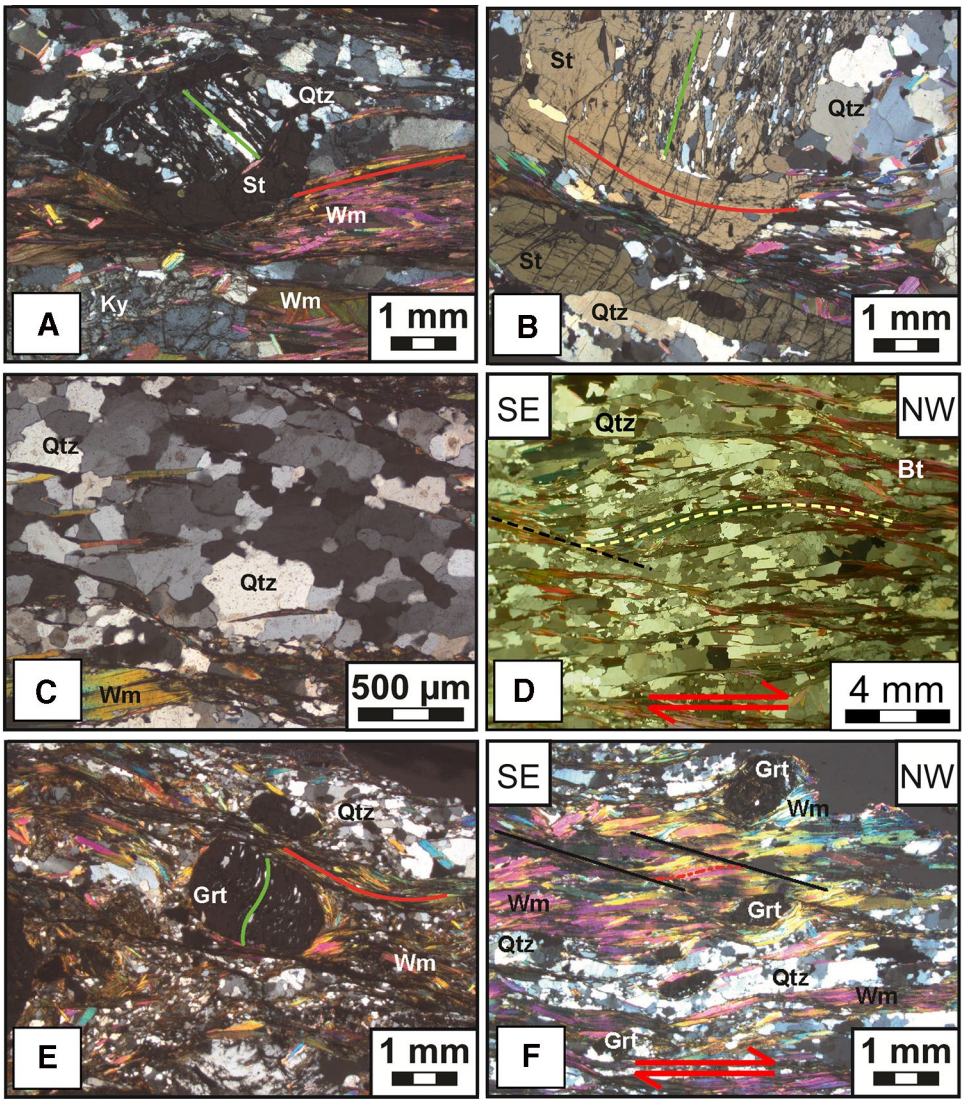

Fig. 7 **a** Staurolite porphyroclast in kyanite-bearing micaschist with an internal foliation S_1 defined by quartz + white mica (green line). The porphyroclast is wrapped by the external foliation S_2 (red line) defined by quartz + white mica (XPL); **b** staurolite porphyroblast, in staurolite-bearing micaschist, showing two stages of growth: an inter-tectonic core with an internal foliation S_1 (green line) and a syn-tectonic rim with an internal foliation S_2 (red line) in continuity with the external one (XPL); **c** deformed quartz in staurolite-bearing micaschist showing lobed and irregular boundaries indicative of grain boundary migration; **d** S-C' fabric in the mylonitic gneiss of the Cavalaire Fault showing a top-to-the-NW sense of shear (C' is marked by a black dashed line, S plane is marked by a yellow dashed line); **e** garnet within garnet-bearing micaschist, showing an internal S_1 foliation defined by elongated quartz (green line), wrapped by an external S_2 foliation (red line) defined by quartz + white mica (XPL); **f** S-C' fabric (S plane is marked by red dashed line, C' marked by black lines) pointing a top-to-the NW sense of shear in garnet-bearing micaschist (XPL)

Table 1 Summary table of the vorticity data obtained with the C' shear band method: number of data (N), angle between C' planes and the shear zone boundary (ν), Wk value (Wk), angles between the maximum ISA in the horizontal plane and the shear zone boundary (θ)

Sample	N	ν(°)	Wk	θ(°)
MTM10	19	32	0.44	13
CD4	4	28	0.55	17
MTM11	19	30	0.50	14
MTM12	29	32	0.44	13
CD6	6	32	0.44	13
CL1	9	32	0.44	12
SL3	6	23	0.68	21
MTM15a	33	32	0.44	13
M2	19	32	0.44	13
SL6	5	33	0.40	12
MTM9	23	29	0.53	16
SL5	27	34	0.37	11

strain ellipsoid (Law 2010). Applying the correction of Law (2010), accounting deviations from plane strain, a stretching parallel to the transport direction of 41% and 40% were obtained for M2 and SL5 samples (Fig. 10c), respectively.

Petrochronology

Four samples (Fig. 2) were selected for an in-situ microstructurally constrained monazite U-Th-Pb petrochronology. Petrochronological data were obtained following the analytical procedure reported in Braden et al. (2017 and references therein). Selected samples were polished, C-coated and inspected using a Scanning Electron Microscope (JEOL JSM IT300LV) hosted at the University of Torino (Italy), to observe monazite microstructural position, internal features and zoning in back-scattered electron (BSE). X-Ray compositional maps (for Y, Ce, Pr, Th, La, P, Ca, U) and chemical

Table 2 Summary table of the vorticity data obtained with the stable porphyroclasts method: number of data (*N*), minimum critical axial ratio (Rc_{min}), maximum critical axial ratio (Rc_{max}), mean critical axial ratio (Rc_m), minimum value of Wk (Wk_{min}), maximum value of Wk (Wk_{max}), mean value of Wk (Wm)

Sample	*N*	Rc_{min}	Rc_{max}	Rc_m	Wk_{min}	Wk_{max}	Wm
M2	418	1.38	1.42	1.40	0.31	0.34	0.32
SL5	172	1.73	2.20	1.96	0.50	0.66	0.58

analyses were acquired with an electron microprobe (JEOL 8200 Super Probe) hosted at the University of Milano (Italy), following the procedure given in Montomoli et al. (2013), to highlight compositional zoning in monazite grains. BSE images showing monazite textural position, internal features and related chemistry are reported in the online resource 4 and 5, respectively.

Monazite was analyzed directly in thin section using the Laser Ablation Split Stream (LASS) method at the University of California Santa Barbara. Spot location was guided with the aid of X-ray compositional maps. Instrumentation consists of a Photon Machines 193 nm ArF Excimer laser and 'HelEx' ablation cell coupled to a Nu Instruments

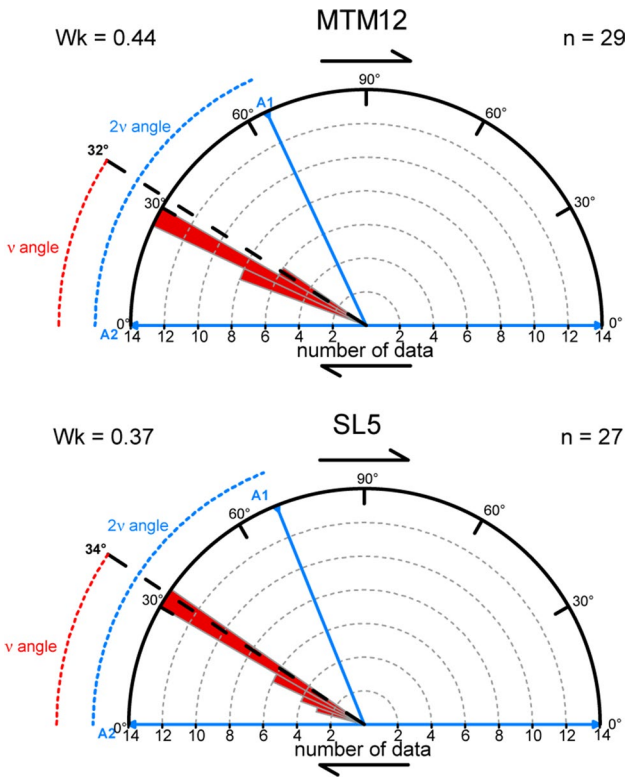

Fig. 8 Examples of polar histograms (for sample MTM12 and SL5) used to derive the angle ν and the corresponding kinematic vorticity. A1 = flow apophysis 1; *A2* flow apophysis 2; *n* total number of data; *Wk* kinematic vorticity number. Dashed line represents the bisector of the angle between A1 and A2 apophyses. The full dataset is reported in online resource 1

HR Plasma high-resolution multi-collector MC-ICP-MS (U, Th, and Pb isotopes) and an Agilent 7700S Quadrupole ICP-MS (major and trace elements). Methods in this study follow those outlined in Kylander-Clark et al. (2013) with modifications outlined in McKinney et al. (2015). Monazite was ablated using a 7 µm diameter spot at 3 Hz repetition rate for 107 shots at a laser fluence of 1.5 J/cm^2, resulting in craters that are ~ 4 µm deep.

Data reduction, including corrections for baseline, instrumental drift, mass bias, down-hole fractionation as well as age calculations were carried out using Iolite v. 2.5 (Paton et al. 2010). Background intensities and changes in instrumental bias were interpolated using a smoothed cubic spline while down-hole inter-element fractionation was modeled using an exponential function. Statistics for baselines, on peak intensities and isotopic ratios were calculated using the mean with a 2.S.D. outlier rejection. Concordia and weighted mean date plots were calculated in Isoplot v.3 (Ludwig 2003) using the ^{238}U and ^{235}U decay constants of Jaffey et al. (1971) and the ^{232}Th decay constant of Amelin and Zaitsev (2002). All uncertainties are quoted at 2σ and include contributions from the external reproducibility of the primary reference material for the ^{206}Pb/^{238}U ratios and ^{208}Pb/^{232}Th ratios. The full dataset is presented in the online resource 6.

Monazite U-Th/Pb data was normalized to '44,069' (424 Ma ^{207}Pb/^{235}U ID-TIMS age, Aleinikoff et al. 2006), employed to monitor and correct for mass bias as well as Pb/U and Pb/Th down-hole fractionation. To monitor data accuracy, two a reference monazite FC-1 (55.7 Ma ^{206}Pb/^{238}U ID-TIMS age, Horstwood et al. 2003) was analyzed concurrently (once every ~ 7 unknowns) and mass bias- and fractionation-corrected based on measured isotopic ratios of the primary reference material. During the analytical period, 11 analyses of FC-1 gave a weighted mean ^{206}Pb/^{238}U date of 57.5 ± 0.4 Ma, MSWD = 1.1, and a weighted mean ^{208}Pb/^{232}Th date of 54.7 ± 0.5 Ma, MSWD = 0.96 (2σ). Based on the long-term reproducibility of multiple secondary reference minerals, trace element concentrations are accurate to 3–5% (2σ). The analysis of the microstructural position of the monazite, combined with its chemical composition, in a system in which they are associated with garnet, as in our samples, help to understand

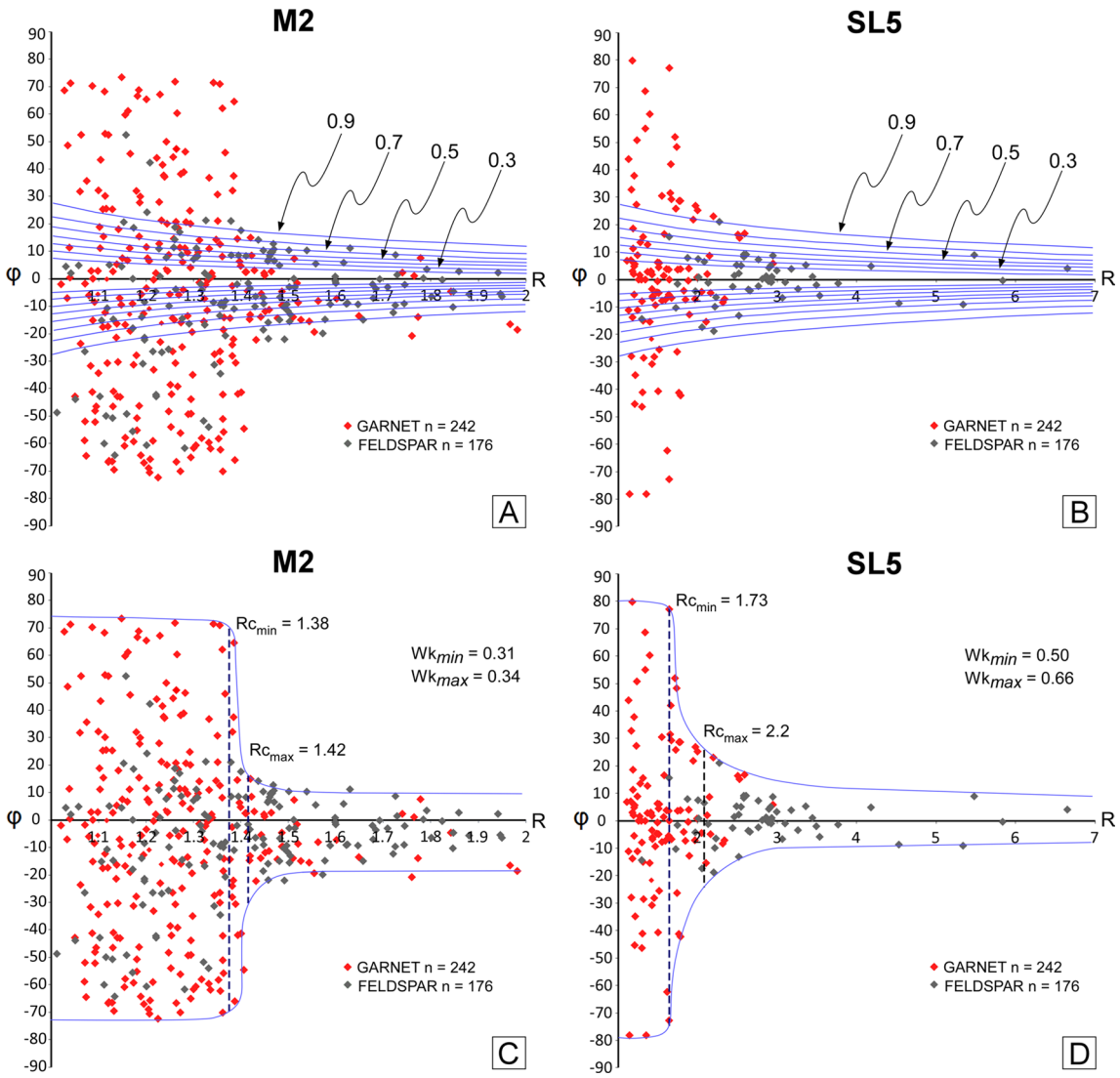

Fig. 9 **a** Mulchrone test (Mulchrone 2007a, b) for sample M2; **b** Mulchrone test (Mulchrone 2007a, b) for sample SL5. Blue curves represent the expected distribution of porphyroclasts, at different Wk values, reaching a stable position in the presence of a clast/matrix-slipping interface. In both samples the distribution of porphyroclasts does not fit these curves, revealing that no significant slip between porphyroclasts and matrix occurred. **c** Graph used to determine the minimum and maximum critical axial ratio (Rc_{min} and Rc_{max} respectively) and the related Wk for sample M2; **d** Graph used to determine the minimum and maximum critical axial ratio (Rc_{min} and Rc_{max} respectively) and the related Wk for sample SL5. R aspect ratio of the porphyloclasts; φ angle between the major axis of the porphyroclast and the mylonitic foliation

when the two phases have grown during the deformation and metamorphic history.

Garnet has a major control on the heavy rare earth elements (HREE) and Y budget in the system (Engi et al. 2017 and references therein). In a closed system, garnet growth will fractionate HREE and Y from the system and thus reduces their availability for monazite (Foster et al. 2002; Hermann and Rubatto 2003; Buick et al. 2006; Rubatto et al. 2006). In contrast, garnet breakdown will release HREE and Y, which can then be redistributed in the monazite growing at the same time. So, during retro-metamorphism, monazite showing increasing values of HREE and Y is expected (Pyle and Spear 1999; Pyle et al. 2001; Williams et al. 2007; Iaccarino et al. 2017). The ratio of Gd to Yb is also useful to approximate the behavior of HREE: a decreasing Gd/Yb indicates garnet breakdown whereas an increasing Gd/Yb indicates garnet growth or growth of monazite in the presence of stable garnet (Braden et al. 2017). Moreover, Eu anomaly can be used as a proxy for monitoring the timing of melt crystallization and abundance of K-feldspar (Braden et al. 2017; Rubatto et al. 2013). Since the main mylonitic foliation in the studied samples developed during decreasing temperature conditions, after a prograde Barrovian stage (Schneider et al.

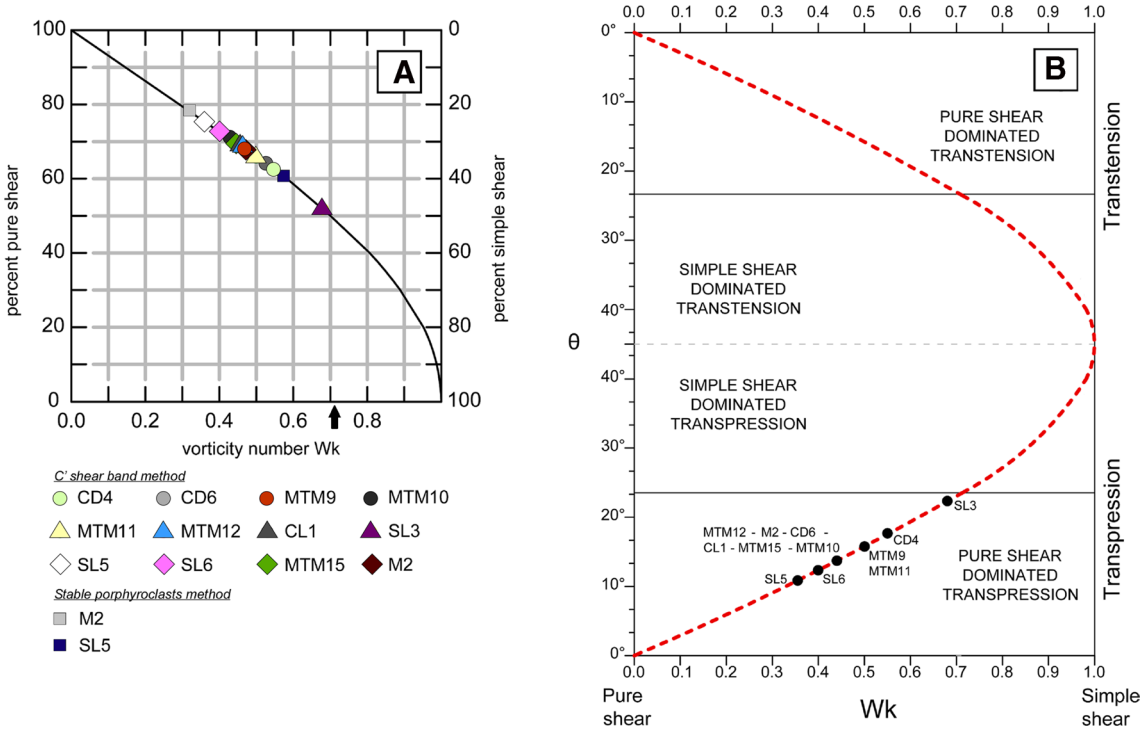

Fig. 10 **a** Percentage of pure shear and simple shear in the study samples in relation to the calculated Wk values. Samples are highlighted with different colors and symbols: dots, triangles and rhombs are results of Wk based on C' shear band method (Kurz and Northrup 2008), whereas squares are the vorticity results based on the stable porphyroclasts method. Black arrow points Wk = 0.71 where equal contribution of simple shear and pure shear is realized (see text); **b** Relationships between the orientation of the maximum Instantaneous Stretching Axis (ISAmax) with respect to the shear zone boundary (angle θ) related to the kinematic vorticity number Wk (modified after Fossen and Tikoff 1993; Fossen et al. 1994). All the study samples fall in the pure shear-dominated transpression field

2014), all these chemical proxies (e.g. Y + HREE zoning, the Gd/Yb ratio, REE patterns) coupled with grain textural position and zoning, guided the interpretation of monazite data with respect to the prograde and/or retrograde stages.

Results

A total of 17 monazites grains (see online resource 3), representative of the different microstructural position of monazite and of their chemical variability, were selected. Examples of the main features of selected monazite are reported in Fig. 12. In sample CD1, five grains (Mnz1, Mnz3, Mnz3b, Mnz4, Mnz5) lie along the S_2 foliation or are included within syn-kinematic biotite and white mica; one grain (Mnz6) is included in plagioclase porphyroclast and one grain (Mnz7) is within staurolite porphyroclast. In sample CD6a, four grains (Mnz1, Mnz9b, Mnz12, Mnz22) lie along the S_2 foliation. In sample MTM10, two grains (Mnz30, Mnz32) along the S_2 foliation and one grain (Mnz8) included in syn-kinematic biotite were chosen. In Sample SL6 we selected one grain (Mnz8) included in a garnet porphyroclast and two grains (Mnz9, Mnz10) included in syn-kinematic white mica on the S_2.

Monazite grains commonly show complex, but similar among samples, Y zoning as highlighted by microprobe chemical mapping (Fig. 12 and online resource 7). We recognize three main compositional domains: (1) high-medium-Y cores (between ~ 0.7 and ~ 1.5 wt % of Y_2O_3); (2) low-Y cores (between ~ 0.1 and ~ 0.5 wt % of Y_2O_3); (3) high-Y rims (between ~ 1.3 and ~ 2.5 wt % of Y_2O_3). Monazites included in garnet (Mnz8, sample SL6), staurolite (Mnz7, sample CD1) and plagioclase (Mnz6, sample CD1) do not show high-Y rims. The Y content in these grains, included in Barrovian minerals, decreases from core to rim. Monazites along the main foliation, or included in syn-kinematic minerals, generally present all the three compositional domains described above (Mnz1, Mnz3, Mnz3b, Mnz4, Mnz5, sample CD1; Mnz1, Mnz9b, Mnz12, Mnz22, sample CD6a; Mnz9, Mnz10, sample SL6) or show an homogeneous high-Y composition (Mnz8, Mnz30, Mnz32, sample MTM10) with Y_2O_3 content variable between ~ 1.9 and ~ 2.5 wt %, comparable with the amount of Y_2O_3 in the high-Y rims.

Petrochronological data for all samples and reference materials are reported in online resource 6 and online resource 7. The relationships between age, Y content, Gd/

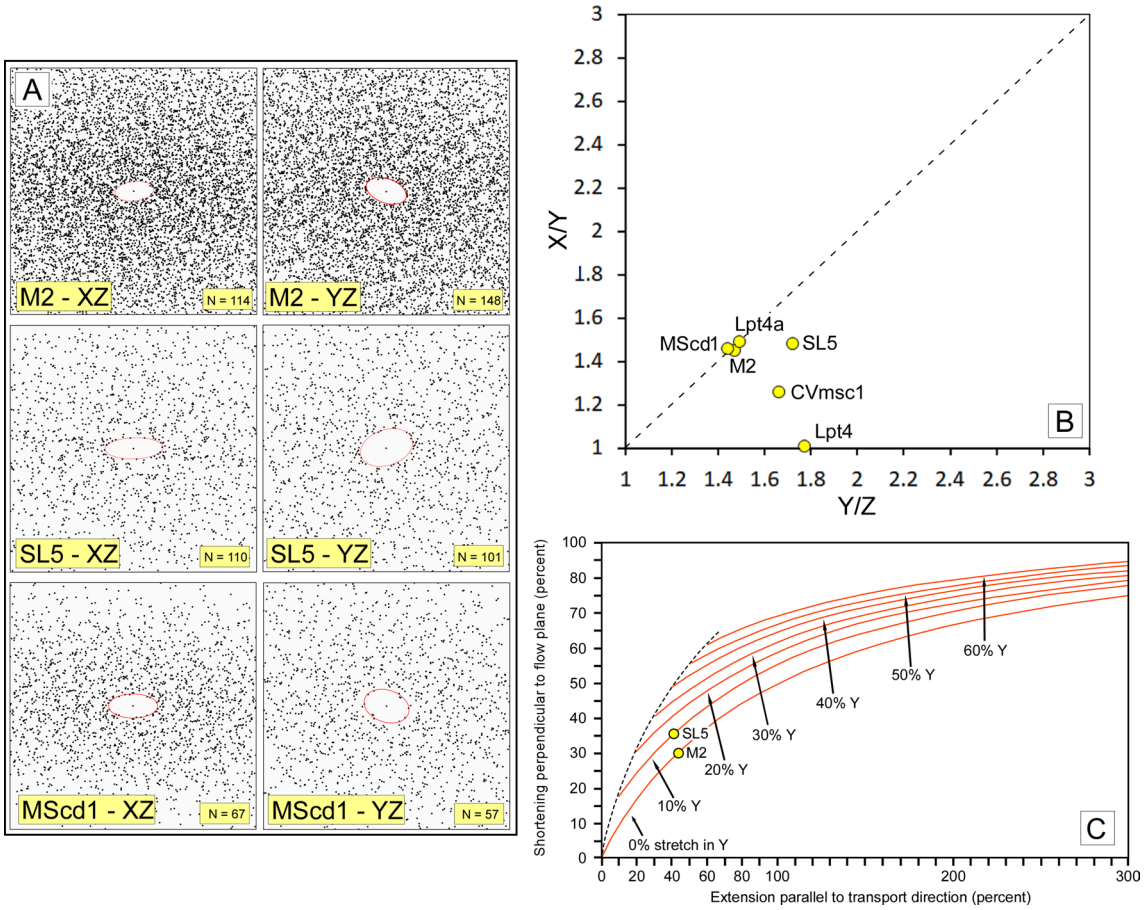

Fig. 11 Results of finite strain analysis: **a** Fry graphs, based on the center-to-center method, for the XZ and YZ sections of the finite strain ellipsoid for selected samples (M2, SL5, MScd1). The full dataset is reported in online resource 2, N number of centers considered in the analysis; **b** Flinn diagram showing the position in the apparent flattening field of the study samples (dots); **c** curves representing the shortening perpendicular to flow plane versus extension in transport direction for general flattening with 0–60% stretch along Y (modified from Law 2010). Dots are samples M2 and SL5)

Yb ratio and REE pattern normalized to chondrite (normalization values after McDonough and Sun 1995) of the different compositional domains are reported in Fig. 13. The $^{206}Pb/^{238}U$ and $^{208}Pb/^{232}Th$ ages are generally concordant. The average $^{206}Pb/^{238}U$ age for each sample is reported in Fig. 14. $^{208}Pb/^{232}Th$ ages range from 344 ± 5 Ma to 323 ± 4 Ma, whereas $^{206}Pb/^{238}U$ ages range from 341 ± 4 Ma to 325 ± 5 Ma. Taking into account the microstructural position of the grains and the chemical composition of the dated domains, we distinguish different groups/populations of ages. Ages older than ~ 340 Ma occur in both the high and low-Y cores of the monazites included in the Barrovian minerals and in the matrix. A second group of ages of ~ 333 Ma was obtained from medium–low-Y mantle. High-Y rims, a feature observed only in matrix grain, generally return ages of ~ 323 Ma. We thus observe a good correlation between ages and Y contents from cores to rims (Fig. 13), in monazite grains. Moreover, younger ages in the rims are coupled with low Gd/Yb ratios (Fig. 13). In samples SL6, CD6 and CD1, we recognized an increase of the HREE content from the cores to the rims while in sample MTM10 there is no such variation (Fig. 13). In samples MTM10 and CD6 the REE distribution highlight a negative Eu anomaly.

Discussion

Geometry and kinematics of the CF

The CF marks the boundary between external and internal zones, affecting both micaschist of the biotite-kyanite zone (Bormes unit) and migmatite (La Garde-Freinet unit). In mylonites from the external zone (Bormes unit) syn-kinematic growth of biotite and white mica along the S_2 foliation is recognized. F_2 folds in the external zone and the mylonitic foliation developed during the same amphibolite-facies metamorphism (M_2 metamorphic stage of Schneider et al. 2014). Barrovian index minerals mainly grew

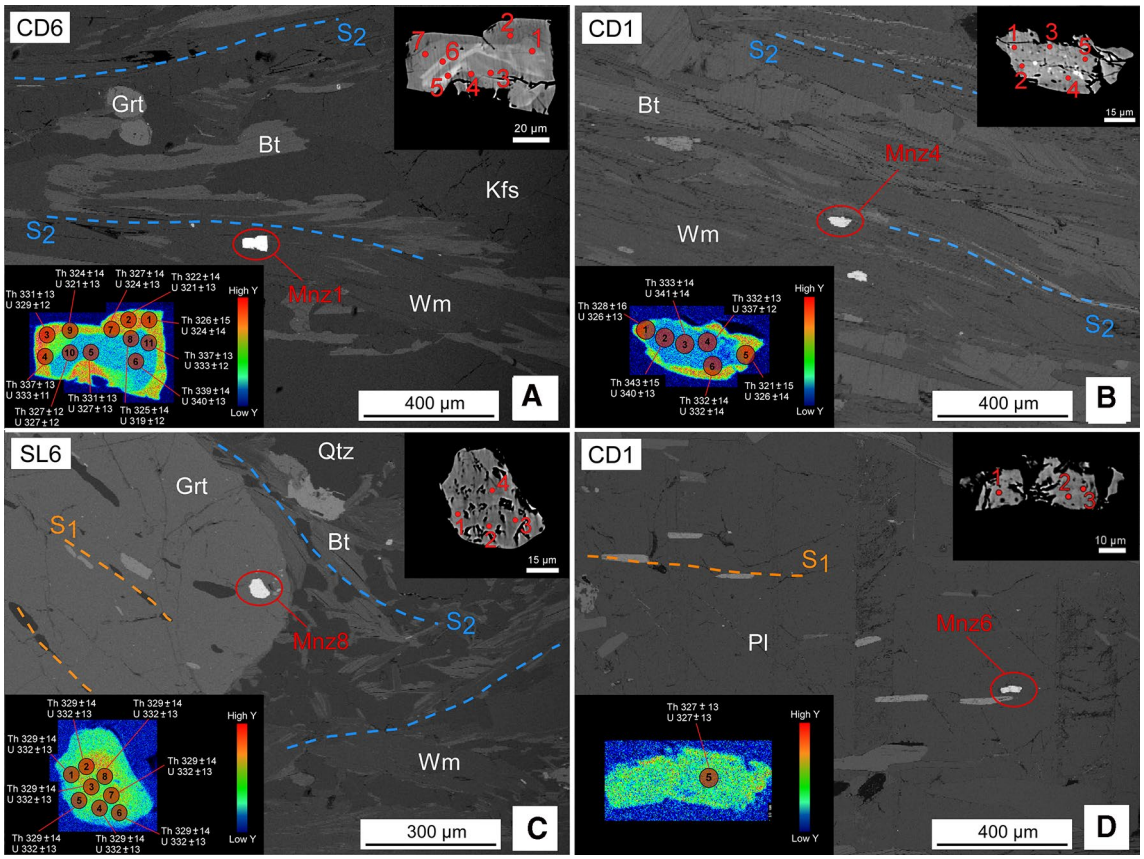

Fig. 12 Examples of textural position and zoning of monazite grains selected for in situ dating. Compositional map of Y shows the spot location and the corresponding $^{208}Pb/^{232}Th$ (Th) and 207-corrected $^{206}Pb/^{238}U$ (U) ages. In the BSE image of the grain, the position of the electron microprobe chemical analysis (red spots) is indicated. **a** Mnz1 in sample CD6, laying along the main S_2 foliation; **b** Mnz4 in sample CD1, located along the main S_2 foliation; **c** Mnz8 in sample SL6, included in garnet porphyroclast; **d** Mnz6 in sample CD1, included in plagioclase porphyroclast

between the collisional (D_1, M_1 metamorphism according to Schneider et al. 2014) and transpressional tectono-metamorphic event (M_2–M_3 metamorphism according to Schneider et al. 2014). However, we documented how that part of the staurolite growth is syn-kinematic during transpression (Fig. 7b). The observed blastesis-deformation relationships between Barrovian minerals and transpression-related non-coaxial shearing in the MTM appear strikingly similar to that reported along the Posada Asinara Line in northern Sardinia (Carosi and Palmeri 2002; Iacopini et al. 2008).

We find no unambiguous evidence of previously reported top-to-the-E-SE thrusting as described by Bellot et al. (2002) and Schneider et al. (2014), likely because its highly overprinting during transpression both in the CF and within the internal zone. Hence, we do not describe three deformation phases (D_1 frontal collision, D_2 backthrust and D_3 transpression as in Schneider et al. 2014) and D_2 in this work (related to the transpression) corresponds to D_2–D_3 of Schneider et al. (2014). Kinematic indicators, both at the meso and microscale, point to a top-to-the-NW sense of shear in agreement with Schneider et al. (2014).

During transpression, the internal zone was characterized by high-temperature metamorphism and widespread partial melting (Schneider et al. 2014). These metamorphic conditions are in agreement with the occurrence of grain boundary migration as the main dynamic recrystallization mechanism of quartz, indicative of a deformation temperature range higher than 500° C. Feldspar in this zone, shows evidence of ductile deformation, with temperature higher than ~ 450° C (Passchier and Trouw 2005). The occurrence of brittle fractures in feldspar could testify a decreasing temperature during deformation, as suggested by Bellot et al. (2002), Bellot (2005) and Schneider et al. (2014), or a subsequent brittle overprint. The first hypothesis is supported by the observation that fractures are at a high-angle to the main foliation and are therefore compatible with the same shortening and stretching directions. Furthermore, local incipient subgrain rotation recrystallization, overprinting GBM in quartz has been recognized in the

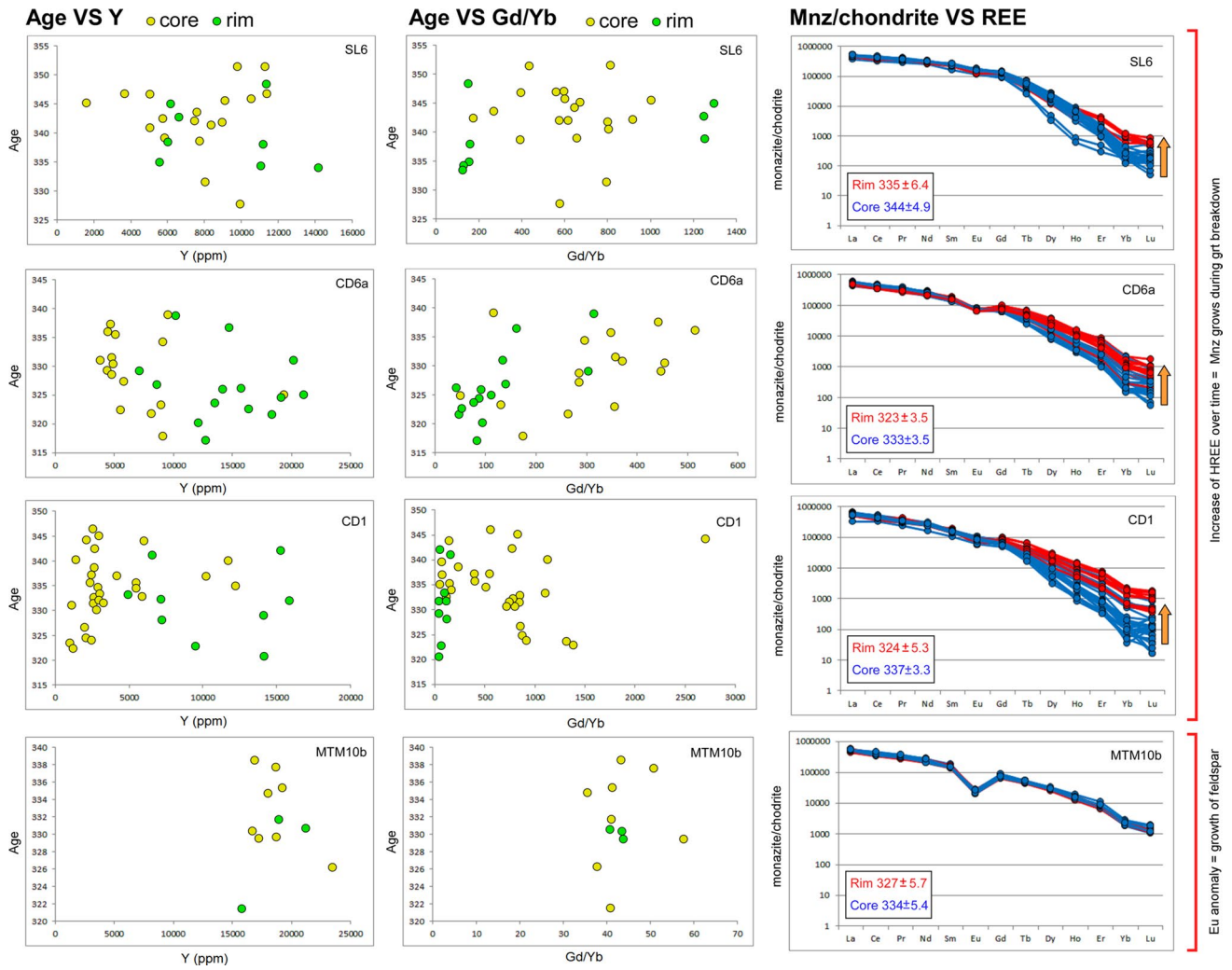

Fig. 13 Trace element characterization of the dated monazite crystals: in the left column the age vs Y content (ppm) is indicated; in the central column the age vs Gd/Yb ratio is given; on the right column chondrite normalized (based on values of McDonough and Sun 1995) REE patterns of dated monazites are shown. Average age for rims and cores are also reported

rocks of the CF, supporting that dynamic recrystallization continued at lower temperatures (Law 2014), following the thermal climax.

Kinematic vorticity analysis allows us to reveal that deformation along the CF occurred under general shear condition with a major component of pure shear acting together with simple shear. The presence, in migmatite of both dextral and sinistral kinematic indicators agrees with a high component of pure shear during deformation (Passchier and Trouw 2005; Fossen 2016).

Finite strain data, suggest a general flattening in agreement with a pure shear-dominated transpression (Fossen and Tikoff 1993; Fossen et al. 1994; Fossen 2016). The general flattening regime is also well compatible with the observation, at outcrop scale, of boudinaged levels occurring in both XZ and YZ sections of finite strain ellipsoid.

According to Schneider et al. (2014), the transpression event (their D_3 event) occurred during the doming of the internal zone. Schneider et al. (2014) hypothesized that the CF firstly developed as a backthrust (their D_2 event) with a top-to-the-E-SE sense of shear. Our field and kinematic data are compatible with a reactivation of the CF as a transpressional shear zone further reoriented and finally reactivated as a normal sense shear zone (top-to-the W sense of shear). During transpression the CF acquired a steeply dipping attitude with a component of pure shear accommodating the exhumation of the internal zone (Fig. 15, stage 1). This kinematic framework is in agreement with both the transpressional models proposed by Sanderson and Marchini (1984) and Fossen et al. (1994) and it could also account for the horizontal shortening pointed out by Schneider et al. (2014) during the building up of the orogen.

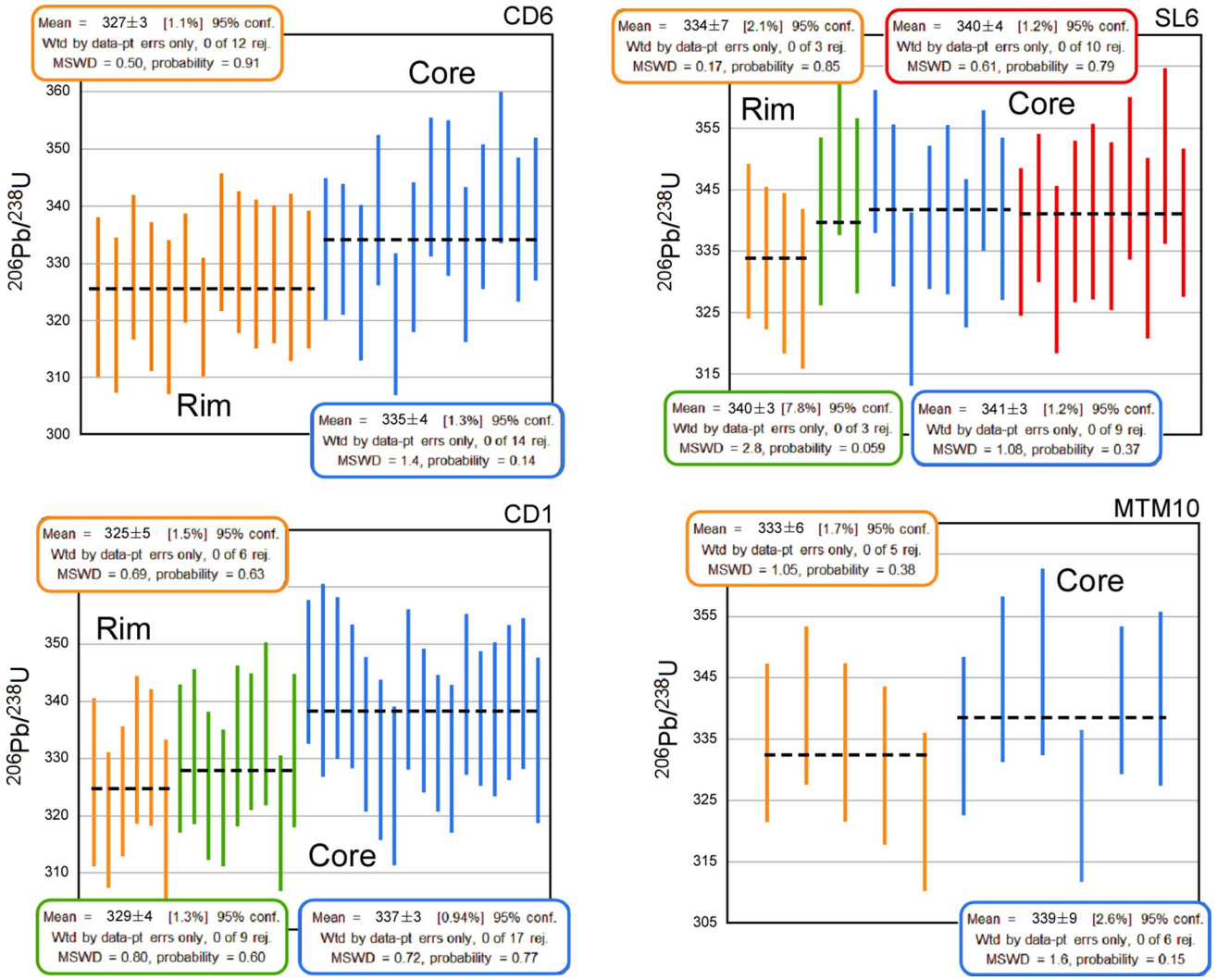

Fig. 14 Distribution of 207-corrected $^{206}Pb/^{238}U$ ages. Data are grouped according to the position of the spot within the grain, colors of the bars are organized according to the Y content: red = high-Y domain in the core of the grain; blue = low-Y domain in the core of the grain; green = medium-Y domain in the core of the grain or in an intermediate position between core and rim (mantle); orange = high-Y domain in the rim of the grain. MSWD = mean square weighted deviates

In the two study areas the stretching lineation L_2 is steeply dipping, but in other sectors of the Maures Massif L_2 is sub-horizontal or slightly plunging (Bellot et al. 2002). A similar structural setting was described in the Asinara Island (Sardinia) by Iacopini et al. (2008) in the northwesternmost outcrops of the Posada Asinara Line. In a transpressive system at a constant strain rate, the orientation of the stretching lineation is a function of time and vorticity number. The orientation of the stretching lineation can change over time during ongoing deformation and strain accumulation (see Iacopini et al. 2008 for a complete review). Iacopini et al. (2008), discussing this topic along the transpressive Posada–Asinara Line, argue that in the case of a sub-vertical lineation, the shear zone will be subjected to vertical extrusion.

The geometry and kinematics of the CF is in accordance with a nearly-vertical attitude of the shear zone developed in transpressional regime in a collisional orogen, allowing the relative normal movement and exhumation of the surrounding rocks. Thompson et al. (1997) demonstrated that compressional forces could sustain the vertical channelized exhumation of the lower crust along sub-vertical shear zones. Therefore, if the CF suffered verticalization, the vertical extrusion could have triggered exhumation and later gravitational instability with development of late folds (F_3) and brittle-ductile reactivation with normal kinematic (Fig. 15, stage 2). At this stage, deformation took place at upper crustal levels in a prevalent brittle regime. Even so, preserved ductile features of sheared rocks acquired during the initial stage of transpression are still recognizable.

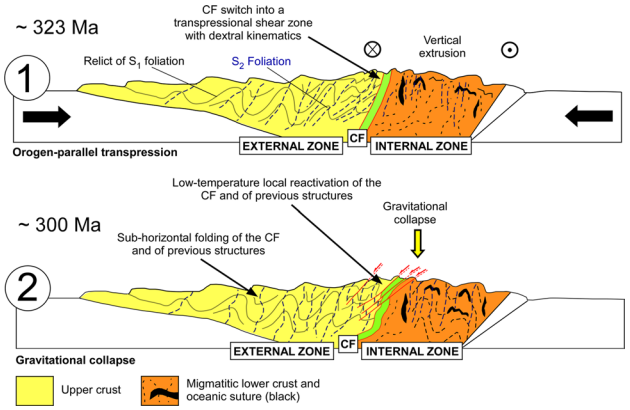

Fig. 15 Sketch of the structural evolution of the Cavalaire Fault located at the boundary between the internal and external zones of the Variscan belt in the MTM. (1) onset of orogen-parallel transpression with development of D_2 folds and associated S_2 foliation. Cavalaire Fault evolved into a transpressive shear zone during the retro-wedge building and, because of the high pure shear component, it suffered verticalization that allowed channelized vertical exhumation of the middle-lower crust; (2) gravitational collapse induced by vertical extrusion generates sub-horizontal open folds and partially reactivated the CF under low-temperature conditions

The geometry of the structures in the study area is further complicated by a later, post-Variscan N-S shortening that resulted in sporadic formation of an S_4 crenulation cleavage. The present-day geometry is therefore the result of a complex and polyphase deformation history from late- to post-Variscan time.

Timing of deformation

A compilation of the existing U-(Th)-Pb time constraints related to the Variscan evolution of the Maures Massif is reported in Table 3. Our new monazite petrochronology data, constrains the timing of shearing along the CF. Microstructural position, texture, zoning and chemical analysis highlight a complex history of monazite growth during the tectono-metamorphic history. A first group of monazite (Mnz1) grew during prograde metamorphic conditions. This is supported by the decreasing Y content from cores to rims, by the low HREE content and by the high Gd/Yb ratio that are a consequence of garnet growth. A second group of monazite (Mnz2) shows high-Y, high-HREE content and low Gd/Yb ratio pointing a growth during retro-metamorphism and garnet breakdown. Mnz2 grows as tiny rims around Mnz1 when the last one is not included/shielded in Barrovian porphyroclasts or as a new grain along the main S_2 foliation with a homogeneous high-Y composition. Since prograde metamorphism is associated with the frontal collisional stage, whereas the retro-metamorphism is related to the transpressional deformation (Schneider et al. 2014; Oliot et al. 2015), the obtained ages for Mnz1 and Mnz2 allow us to constrain these two tectonic events. The REE patterns (Fig. 13) highlight also the presence of an Eu anomaly in the samples MTM10 and CD6, collected close to the internal zone. This is an evidence of the growth of feldspar during partial melting and allows to directly link the anatexis with the transpressional deformation (Schneider et al. 2014; Oliot et al. 2015). Ages from the Mnz2 indicate a deformation active at ~ 323 Ma. Older ages, detected in the cores of monazite, range between ~ 340 Ma and ~ 333 Ma, are in agreement with the timing of the prograde metamorphism from 382 ± 11 Ma (Middle Devonian) to 331 ± 5 Ma (Late Visean) (Table 3; Oliot et al. 2015). According to the evolution of a garnet-monazite system (Pyle and Spear 1999; Pyle et al. 2001; Williams et al. 2007) during prograde metamorphism high-Y + HREE cores are expected to grow just before medium to low-Y cores (Pyle and Spear 1999), and therefore older ages are expected from the former. We detected little difference in the absolute ages of high- and low-Y cores (340 ± 4 Ma and 341 ± 3 Ma, respectively, Fig. 14), this could reflect a rapid phase of prograde metamorphism during ongoing collision.

The CF in the framework of the Variscan belt

The MTM shows striking similarities with the tectono-metamorphic evolution of the Variscan basement in northern Sardinia (Corsini and Rolland 2009; Rossi et al. 2009; Schneider et al. 2014; Edel et al. 2018).

Previous interpretations of the structural asset of the MTM considered the Joyeuse–Grimaud Fault as the suture zone and the major tectonic boundary in the massif (Vauchez and Bufalo 1985; 1988; Morillon et al. 2000; Bellot 2005). A similar interpretation has been proposed for the Posada–Asinara Line in northern Sardinia (Cappelli et al. 1992; Carmignani et al. 1992, 1994). Accordingly, the two shear zones were regarded to be in continuity. The Posada–Asinara Line was later interpreted as an intracontinetal major late-Variscan sub-vertical transpressional shear zone separating two orogenic domains with different metamorphic imprints (Carosi and Palmeri 2002; Carosi et al. 2012). Schneider et al. (2014) recognized that in the MTM the suture is located within the internal zone as a dismembered zone and that the Joyeuse–Grimaud Fault is a simple strike-slip shear zone confined within this zone. Therefore, in the MTM, the Joyeuse–Grimaud Fault can no longer be considered the main boundary between the two orogenic domains.

The MTM and northern Sardinia show a low- to medium-grade complex and a migmatitic complex, with granitic intrusions, separated by a ductile, transpressive shear zone. Vorticity analysis in the shear zone at both localities confirms the contemporaneous occurrence of simple and pure shear during deformation (Table 4).

Table 3 Synthesis of the available U-(Th)-Pb time constraints, from this work and the literature, related to the Variscan evolution of the Maures Massif

Zone	Unit	Rock type	Age (Ma)	Mineral	Method	Interpretation	Tectonic setting	References
External	Bormes	Paragneiss	367 ± 13	Monazite	EPMA in situ	Prograde metamorphism, underthrusting	Continental collision	Oliot et al. (2015)
External	Bormes	Micaschist	352 ± 5	Monazite	EPMA in situ	Prograde metamorphism, nappes stacking	Continental collision	Oliot et al., (2015)
External	Bormes	Othogneiss	345 ± 3	Monazite	TIMS	Age of deformation	Continental collision	Moussavou (1998)
External	Bormes	Othogneiss	344 ± 15	Zircon	TIMS	Age of deformation	Continental collision	Moussavou (1998)
External	Bormes	Othogneiss	339 ± 16	Zircon	TIMS	Age of deformation	Continental collision	Moussavou, (2000)
External	Bormes	Paragneiss	335 ± 6	Monazite	EPMA in situ	Prograde metamorphism, backthrusting	Continental collision	Oliot et al. (2015)
Transition	Bormes	Sheared micaschist	335 ± 4	Monazite	LASS in situ	Prograde metamorphism	Continental collision	This study
Transition	Bormes	Sheared micaschist	327 ± 3	Monazite	LASS in situ	Retrometamorphism	Transpression along the Cavalaire Fault	This study
Transition	La Garde-Freinet	Sheared micaschist	340 ± 4	Monazite	LASS in situ	Prograde metamorphism	Continental collision	This study
Transition	La Garde-Freinet	Sheared micaschist	340 ± 3	Monazite	LASS in situ	Prograde metamorphism	Continental collision	This study
Transition	La Garde-Freinet	Sheared micaschist	341 ± 4	Monazite	LASS in situ	Prograde metamorphism	Continental collision	This study
Transition	La Garde-Freinet	Sheared micaschist	334 ± 7	Monazite	LASS in situ	Prograde metamorphism	Continental collision	This study
Transition	Bormes	Sheared micaschist	337 ± 3	Monazite	LASS in situ	Prograde metamorphism	Continental collision	This study
Transition	Bormes	Sheared micaschist	329 ± 4	Monazite	LASS in situ	Prograde metamorphism	Continental collision	This study
Transition	Bormes	Sheared micaschist	325 ± 5	Monazite	LASS in situ	Retrometamorphism	Transpression along the Cavalaire Fault	This study
Transition	Bormes	Sheared paragneiss	339 ± 9	Monazite	LASS in situ	Progade metamorphism	Continental collision	This study
Transition	Bormes	Sheared paragneiss	333 ± 6	Monazite	LASS in situ	Progade metamorphism	Continental collision	This study
Internal	Eastern gneiss	Migmatitic paragneiss	382 ± 11	Monazite	EPMA in situ	Prograde metamorphism, underthrusting	Continental collision	Oliot et al. (2015)
Internal	Eastern gneiss	Migmatitic paragneiss	344 ± 4	Zircon	EPMA in situ	Prograde metamorphism, nappes stacking	Continental collision	Oliot et al. (2015)
Internal	Eastern gneiss	Migmatitic paragneiss	334 ± 3	Zircon	TIMS	Prograde metamorphism,	Continental collision	Moussavou (1998)
Internal	Eastern gneiss	Migmatitic paragneiss	333 ± 3	Monazite	TIMS	Prograde metamorphism	Continental collision	Moussavou, (1998)
Internal	La Garde-Freinet	Diatexite	331 ± 5	Monazite	EPMA in situ	Prograde metamorphism, backthrusting	Continental collision	Oliot et al. (2015)
Internal	Eastern gneiss	Plan-de-la-Tour granite	329 ± 3	Monazite	EPMA in situ	Plan-de-la-Tour granite emplacement	Variscan granitoid emplacement	Oliot et al. (2015)
Internal	Eastern gneiss	Plan-de-la-Tour granite	324 ± 5	Zircon	TIMS	Plan-de-la-Tour granite emplacement	Variscan granitoid emplacement	Moussavou (1998)
Internal	Eastern gneiss	Migmatite leucosome	325 ± 8	Zircon	TIMS	Mineral growth during syn-shear melting	Post-collisional syn-shear Anatexis	Moussavou (1998)
Internal	Eastern gneiss	Migmatite leucosome	310 ± 10	Zircon	SHRIMP	Mineral growth during syn-shear melting	Post-collisional syn-shear Anatexis	Duchesne et al. (2013)

EPMA electron-probe micro-analyses, *LASS* laser ablation split system, *SHRIMP* Sensitive high-resolution ion microprobe, *TIMS* thermal ionization mass spectrometry

Table 4 Table summarizing the main features of the Cavalaire Fault in the Maures Massif (this work), Posada–Asinara Line in northern Sardinia (Carosi and Palmeri 2002; Frassi et al. 2009; Carosi et al. 2012) and Ferriere–Mollières shear zone in the Argentera–Mercantour Massif (Simonetti et al. 2017, 2018)

	Maures Massif	North Sardinia	Argentera Massif
Main structure	Cavalaire Fault	Posada–Asinara shear zone	Ferriere–Mollières shear zone
Involved lithotypes	Medium- to high-grade schist, gneiss and migmatite	Medium- to high-grade schist, gneiss and migmatite	Migmatite
Sense of shear	Top-to-the NW	Top-to-the W-NW	Top-to-the SE
Age of shearing	~323 Ma (U-Th-Pb on monazite)[1]	~325–~300 Ma (U-Th-Pb on monazite and zircon)[3]	~340–~320 Ma (U-Th-Pb on monazite)[6]
Syn-shear metamorphism	Retrometamorphism from Amphibolite-facies to greenschist-facies[1, 2]	Retrometamorphism from Amphibolite-facies to greenschist-facies[4]	Retrometamorphism from HT Amphibolite-facies to greenschist-facies[6]
Kinematic of the flow			
C' shear band method	Pure shear-dominated transpression (p.s. 75%—52%)[1]	–	Pure shear-dominated transpression to simple shear-dominated transpression (p.s. 86%—33%)[6]
Stable porphiroclasts method	Pure shear-dominated transpression (p.s. 78–62%)[1]	Pure shear-dominated transpression to simple shear-dominated transpression (p.s. 64–48%)[4]	Pure shear-dominated transpression (p.s. 63–52%)[7]
Quartz *c*-axis method	–	Simple shear-dominated transpression (p.s 58–13%)[5]	–
Strain geometry	Plane strain to general flattening[1]	Nearly plane strain[5]	Plane strain to general flattening[6, 7, 8]

1: This work; 2: Schneider et al. (2014); 3: Carosi et al. (2012); 4: Carosi and Palmeri (2002); 5: Frassi et al. (2009); 6: Simonetti et al. (2018); 7: Simonetti et al. (2015); 8: Mammoliti (2015); 9: D'addario (2015)

In both Sardinia and MTM deformation linked to the collisional stage can be clearly recognized in the low- to medium-grade metamorphic domain (Carosi and Palmeri 2002; Schneider et al 2014; Montomoli et al 2018; Gerbault et al 2018) and it is followed by a transpressive deformation. This transpressional shear becomes more intense approaching the high-grade migmatitic zone, characterized by contemporary development of folds and shear zones (Carosi and Palmeri 2002; Carosi et al. 2012). A progressive Barrovian metamorphism, approaching the transpressive zone, can be recognized both in Sardinia (from SW to NE; Carmignani et al. 1994) and in the MTM (from W to E; Corsini and Rolland 2009; Schneider et al. 2014; see Fig. 1). In both sectors Barrovian minerals began to grow at the end of the collisional stage and continued to grow syn-kinematically during, at least, part of the subsequent transpressive stage.

In both shear zones transpressive deformation, associated with rocks decompression, developed from amphibolite-facies metamorphism up to greenschist facies (Tab. 4). In both shear zones a general flow regime is observed with the coexistence of simple and pure shear, the latter with a shortening axis normal to the shear zone boundary. Moreover, our petrochronological data and available texturally-controlled geochronological information for northern Sardinia (Carosi et al. 2012; Di Vincenzo et al. 2004) indicate similar timing, both for the prograde and transpressive tectono-metamorphic histories (Table 4). Finally, both the Posada–Asinara Line and the CF are affected by a later gravitational collapse of the belt (Carosi and Palmeri 2002; Schneider et al. 2014) linked to the final exhumation of the mid- lower crust.

The position of the Corsica–Sardinia Block in close continuity with southern France is also supported by new paleomagnetic data (Advokaat et al. 2014) and recent plate tectonics reconstructions of van Hinsbergen et al. (2020), at least since Ladinian time. They did not investigate Mediterranean paleogeography further back in time, but several others reconstruction (Ricci and Sabatini 1978; Elter and Pandeli 2005; Edel 2000; Corsini and Rolland 2009; Rossi et al. 2009; Schneider et al. 2014; Advokaat et al. 2014; Gerbault et al. 2018; Edel et al. 2018; Ballèvre et al. 2018) propose the close correlation between MTM and Corsica–Sardinia Block taking into account paleomagnetic and geological evidences.

The data of this contribution are in agreement with those reconstructions. The observations in this paper suggest that the CF and the Posada–Asinara Line, showing striking similarity in respect to structural architecture, kinematics and timing, may belong to the same network of shear zones that separated the well-defined internal and external zones (Fig. 16) of this sector of the Variscan belt (Vauchez and Bufalo 1985, 1988; Morillon et al. 2000; Carosi and Palmeri 2002; Corsini and Rolland 2009; Schneider et al. 2014). Transpressive deformation, in this portion of the belt, has been attributed to a complex network of dextral shear zones

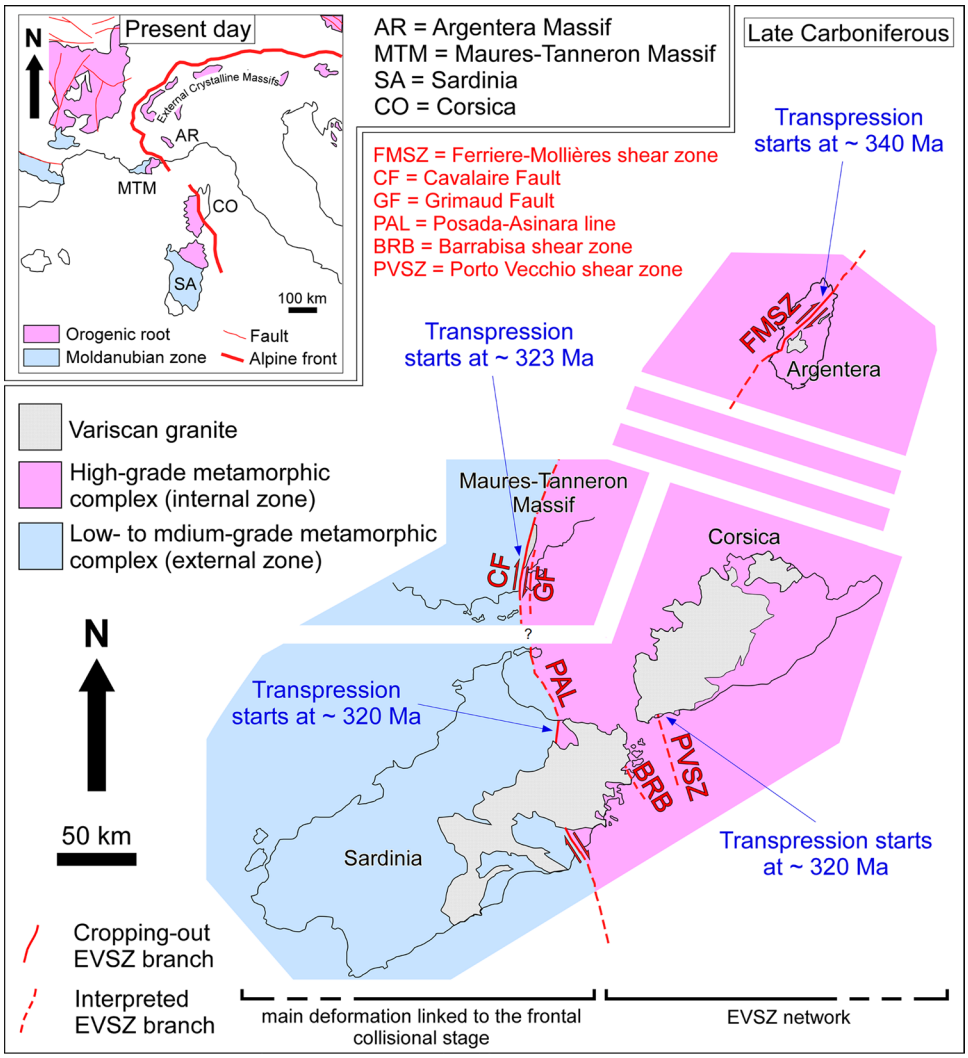

Fig. 16 **a** Structural sketch map of Mediterranean Variscan Europe (modified from Matte 2001) showing present-day relations between Corsica–Sardinia Block, Maures–Tanneron Massif and Alpine External Crystalline Massifs; **b** Sketch of the possible late Carboniferous relationship between Corsica–Sardinia Block, Maures–Tanneron Massif and Argentera Massif (modified after Gerbault et al. (2018); timing of transpression is from Simonetti et al. (2018) for the FMSZ; this work for the CF; Di Vincenzo et al. (2004) and Carosi et al. (2012) for the PAL and Giacomini et al. (2008) for the PVSZ; rotation of the Argentera Massif is from Collombet et al. (2002))

developed at the regional-scale, the EVSZ, running through the Bohemian virgation, Western Alps, southern France and Corsica–Sardinia (Matte 2001; Corsini and Rolland 2009; Carosi et al. 2012; Padovano et al. 2011, 2014; Schneider et al. 2014; Simonetti et al. 2017, 2018, 2020). Our new data fill a gap in the vorticity of the flow, deformation temperature, finite strain and timing of the southern sector of the EVSZ. Variscan intraplate shearing has also been proposed as the main geodynamic settings where the Corsica–Sardinia batholith was generated and emplaced between 325 and 300 Ma (Casini et al. 2015).

Geological, structural and chronological data collected and discussed in this paper can contribute to the debate concerning the reconstruction of the southeastern European Variscan belt and they can be taken into account, to reinforce possible models for the connection of the Corsica–Sardinia Block to southern France before the final break-up of Pangea and the opening of the Western Mediterranean basin (Arthaud and Matte 1977; Ricci and Sabatini 1978; Matte 2001; Rollet et al. 2002; Rosenbaum et al. 2002; Elter et al. 2004; Elter and Pandeli 2005; Bellot 2005; Corsini and Rolland 2009; Advokaat et al. 2014; Edel et al. 2014, 2018; van Hinsbergen et al. 2020; Guerrera et al. 2019).

Conclusions

This work shows that the CF was a pure shear-dominated transpressive ductile shear zone affecting rocks at the boundary between two large-scale structural and metamorphic domains: the external and internal zones in the MTM. The CF played a primary role in the exhumation of the internal zone from the early stages of transpression until later gravitational collapse. Texturally-controlled monazite petrochronology reveals that activity of the CF and the onset of transpression in the MTM occurred at ~ 323 Ma, following the collisional stage occurred at least from 340 up to ~ 333 Ma. Our data indicate close similarities between the

Variscan structural framework and metamorphic evolution for both MTM and Northern Sardinia. The CF is interpreted as a branch of the EVSZ. The results presented here demonstrate the importance of studying regional shear zones with a multidisciplinary approach. Valuable information with regional implications can only be obtained if different and independent techniques are integrated to constrain temperature, absolute timing and deformation in terms of finite strain and kinematic of the flow.

Software

The kinematic vorticity analysis with the stable porphyroclasts method and the finite strain analysis were performed using the software EllipseFit 3.2 by Vollmer (2015). Geochronological data were treated with Isoplot 3.70 (Ludwig 2008).

Acknowledgments Research funded by PRIN 2015 (University of Torino: R. Carosi and University of Torino: C. Montomoli), PRA 2018_41 (C. Montomoli) and funds Ricerca Locale University of Torino (60%, R. Carosi; S. Iaccarino). We thank the Editor Christian Dullo, Philippe Rossi and an anonymous reviewer for their comments that improved the quality of the manuscript.

References

Advokaat EL, van Hinsbergen DJJ, Maffione M, Langereis CG, Vissers RLM, Cherchi A, Schroeder R, Madani H, Columbus S (2014) Eocene rotation of Sardinia, and the paleogeography of the western Mediterranean region. Earth Planet Sci Lett 401:183–195

Aleinikoff JN, Schenck WS, Plank MO, Srogi L, Fanning CM, Kamo SL, Bosbyshell H (2006) Deciphering igneous and metamorphic evens in high-grade rocks of the Wilmington Complex, Delaware: morphology, cathodoluminescence and backscattered electron zoning, and SHRIMP U-Pb geochronology of zircon and monazite. Geol Soc Am Bull 118:39–64

Amelin Y, Zaitsev AN (2002) Precise geochronology of phoscorites and carbonatites: the critical role of U-series disequilibrium in age interpretations. Geochim Cosmochim Acta 66:2399–2419

Arthaud F, Matte P (1977) Détermination de la position initiale de la Corse et de la Sardaigne à la fin de l'orogenesè hercynienne grace aux marqueurs géologiques antémésozoiques. B Soc Geol Fr 19:833–840

Ballèvre M, Manzotti P, Dal Piaz GV (2018) Pre-Alpine (Variscan) inheritance: a key for the location of the future Valaisan Basin (Western Alps).: pre-Alpine (Variscan) inheritance: a key for the location of the future Valaisan Basin (Western Alps). Tectonics 37:786–817

Bard JP, Caruba C (1981) Les séries leptyno-amphiboliques à éclogites relictuelles et serpentinites des Maures, marqueurs d'une paléosuture varisque affectant une croûte amincie? C R Acad Sci Paris, série II 292:611–614

Bellot JP, Bronner G (2000) La tectonique tangentielle à vergence SE du massif des Maures, témoin de chevauchements syn-exhumation? CR Acad Sci Paris, série II 331(10):659–665

Bellot JP, Bronner G, Marchand J, Laverne C, Triboulet C (2002) Chevauchement et détachement dans les Maures occidentales (Var, France). Géologie de la France 1:21–37

Bellot JP (2005) The Palaeozoic evolution of the Maures massif (France) and its potential correlation with other areas of the Variscan Belt: a review. In: Carosi R, Dias R, Iacopini D, Rosenbaum G. (eds) The southern Variscan belt. Journal of the Virtual Explorer, Electronic Edition, ISSN, 19, 1441–8142

Braden Z, Godin L, Cottle JM (2017) Segmentation and rejuvenation of the Greater Himalayan sequence in western Nepal revealed by in situ U-Th/Pb monazite petrochronology. Lithos 285:751–765

Briand B, Bouchardon JL, Capiez P, Piboule M (2002) Felsic (A-Type)-basic (Plume-Induced) Early Palaeozoic bimodal magmatism in the Maures massif (southeastern France). Geol Mag 139:291–311

Buick IS, Hermann J, Williams IS, Gibson RL, Rubatto D (2006) A SHRIMP U-Pb and LA-ICP-MS trace element study of the petrogenesis of garnet–cordierite–orthoamphibole gneisses from the Central Zone of the Limpopo Belt, South Africa. Lithos 88:150–172

Burg JP, Matte P (1978) A cross-section through the French Massif Central and the scope of its Variscan geodynamic evolution. Z Dtsch Geol Ges 109:429–460

Buscail F (2000) Contribution a la compréhension du problème géologique et géodynamique du massif des Maures: le métamorphisme régional modélisé dans le système KFMASH: analyse paragénétique, chémiographie, thermobarométrie, géochronologie Ar/Ar. Unpublished thesis, Université de Montpellier II, France

Cappelli B, Carmignani L, Castorina F, Di Pisa A, Oggiano G, Petrini R (1992) A Variscan suture zone in Sardinia: geological and geochemical evidence. Geodin Acta 5:101–108

Carmignani L, Barca S, Cappelli B, Di Pisa A, Gattiglio M, Oggiano G, Pertusati PC (1992) A tentative geodynamic model for the Hercynian basement of Sardinia. In: Carmignai L, Sassi FP (eds) Contributions to the Geology of Italy with special regard to the Palaeozoic basements. IGCP Project 276, Newsletter 5. Siena, pp 61–83

Carmignani L, Carosi R, Di Pisa A, Gattiglio M, Musumeci G, Oggiano G, Pertusati PC (1994) The Hercynian chain in Sardinia (Italy). Geodin Acta 7:31–47

Carosi R, Oggiano G (2002) Transpressional deformation in northwestern Sardinia (Italy): insights on the tectonic evolution of the Variscan Belt. C R Geosciences 334(4):287–294

Carosi R, Palmeri R (2002) Orogen-parallel tectonics transport in the Variscan belt of northeastern Sadinia (Italy): implications for the exhumation of medium-pressure metamorphic rocks. Geol Mag 139:497–511

Carosi R, Montomoli C, Tiepolo M, Frassi C (2012) Geochronological constraints on post-collisional shear zones in the Variscides of Sardinia (Italy). Terra Nova 24:42–51

Carosi R, D'addario E, Mammoliti E, Montomoli C, Simonetti M (2016) Geology of the northwestern portion of the Ferriere-Mollieres Shear Zone, Argentera Massif, Italy. J Maps 12:466–475

Casini L, Cuccuru S, Puccini A, Oggiano G, Rossi P (2015) Evolution of the Corsica–Sardinia Batholith and late-orogenic shearing of the Variscides. Tectonophysics 646:65–78

Chabrier G, Mascle G (1975) Comparaison des évolutions géologiques de la Provence et de la Sardaigne. Revue de Géographie Pgysique ete de Géologie Dynamique 2(XVII):121–136

Collombet M, Thomas JC, Chauvin A, Tricart P, Bouillin JP, Gratier JP (2002) Counterclockwise rotation of the western Alps since the Oligocene: new insights from paleomagnetic data. Tectonics 21(4):1032. https://doi.org/10.1029/2001TC901016

Compagnoni R, Ferrando S, Lombardo B, Radulesco N, Rubatto D (2010) Paleo-European crust of the Italian western Alps: geological history of the Argentera Massif and comparison with Mont Blanc-Aiguilles Rouges and Maures–Tanneron Massifs. J Virtual Explorer 36:4. https://doi.org/10.3809/jvirtex.2010.00228

Corsini M, Rolland Y (2009) Late evolution of the southern European Variscan belt: exhumation of the lower crust in a context of oblique convergence. C R Geosci 341:214–223

Crevola G, Pupin JP (1994) Crystalline provence: structure and Variscan evolution. In: Keppie JD (ed) Pre-Mesozoic geology in France and related areas. Springer Verlag, Berlin Heidelberg, pp 426–441

Cruciani G, Montomoli C, Carosi R, Franceschelli M, Puxeddu M (2015) Continental collision from two perspectives: a review of Variscan metamorphism and deformation in northern Sardinia. Periodico di Mineralogia 84(3b):657–699. https://doi.org/10.2451/2015PM0455

D'Addario E (2015) Cartografia geologica, analisi strutturale e vorticità cinematica di una zona di taglio regionale: la "Ferriere-Mollères Shear Zone" tra i valloni Forneris e di Pontebernardo (Massiccio dell'Argentera, Alpi Occidentali). Unpublished Thesis, Università degli Studi di Pisa (Italy), pp 203

Dias R, Ribeiro A (1995) The Ibero-Armorican arc. A collision effect against an irregular continent? Tectonophysics 246:113–128

Dias R, Ribeiro A, Romão J, Coke C, Moreira N (2016) A review of the arcuate structures in the Iberian Variscides; constraints and genetic models. Tectonophysics 681:170–194

Dilek Y, Furnes H (2019) Tethyan ophiolites and Tethyan seaways. J Geol Soc Lond 176:899–912

Di Vincenzo G, Carosi R, Palmeri R (2004) The Relationship between Tectono-metamorphic Evolution and Argon Isotope Records in White Mica: Constraints fromin situ ^{40}Ar-^{39}Ar Laser Analysis of the Variscan Basement of Sardinia. J Petrol 45:1013–1043. https://doi.org/10.1093/petrology/egh002

Duchesne JC, Liégeois JP, Bolle O, Vander Auwera J, Bruguier O, Matukov DI, Sergeev SA (2013) The fast evolution of a crustal hot zone at the end of a transpressional regime: The Saint-Tropez peninsula granites and related dykes (Maures Massif, SE France). Lithos 162–163:195–220. https://doi.org/10.1016/j.lithos.2012.12.019

Edel JB (2000) Hypothesis for the Late Variscan clockwise rotation of the Maures–Estérel–Corsica–Sardinia block. New paleomagnetic data from the Plan-de-la-Tour basin (Maures, Provence) and review of the previous data. Géologie de la Fr 1:3–19

Edel JB, Casini L, Oggiano G, Rossi P, Schulmann K (2014) Early Permian 90° clockwise rotation of the Maures–Estérel–orsica–Sardinia block confirmed by new palaeomagnetic data and followed by a Triassic 60° clockwise rotation. Geol Soc Lond Spec Publ 405:1–29

Edel JB, Schulmann K, Lexa O, Lardeaux JM (2018) Late Palaeozoic palaeomagnetic and tectonic constraints for amalgamation of Pangea supercontinent in the European Variscan belt. Earth-Sci Rev 177:589–612

Elter FM, Pandeli E (2005) Structural-Metamorphic correlations between three Variscan segments in Southern Europe: Maures Massif (France), Corsica (France)–Sardinia (Italy), and Northern Appennines (Italy). J Virtual Explor, Electronic Edition, ISSN 162–163:1441–8142

Elter FM, Corsi B, Cricca P, Muzio G (2004) The southwestern Alpine foreland: correlation between two sectors of the Variscan chain belonging to "stable Europe": Sardinia-Corsica and the Maures massif (south-eastern France). Geodin Acta 17:31–40

Engi M, Lanari P, Kohn M J (2017) Significant ages—an introduction to petrochronology: methods and applications. In: Engi M, Lanari P, Kohn MJ (eds) Petrocronology: methods and applications. Reviews in Mineralogy and Geochemistry. doi: 10.1515/9783110561890-002

Fernández-Lozano J, Pastor-Galán D, Gutiérrez-Alonso G, Franco P (2016) New kinematic constraints on the Cantabrian orocline: a paleomagnetic study from the Peñalba and Truchas synclines, NW Spain. Tectonophysics 681:195–208

Flinn D (1962) On folding during three-dimensional progressive deformation. QJ Geol Soc Lond 118:385–433

Fossen H (2016) Structural geology. Cambridge University Press, Cambridge, p 524

Fossen H, Cavalcante GCG (2017) Shear zones—a review. Earth Sci Rev 171:434–455

Fossen H, Tikoff B (1993) The deformation matrix for simultaneous simple shearing, pure shearing and volume change, and its application to transpression-transtension tectonics. J Struct Geol 15:413–422

Fossen H, Tikoff B (1998) Extended models of transpression and transtension, and application to tectonic settings. In: Holdsworth RE, Strachan RA, Dewey JF (eds) Continental transpressional and transtensional tectonics. Geol Soc Lond Spec Publ, 135, pp 15–33

Fossen H, Tikoff B, Teyssier C (1994) Strain modelling of transpressional and transtensional deformation. Norsk Geol Tidsskr 74:134–145

Foster G, Gibson HD, Parrish R, Horstwood M, Fraser J, Tindle A (2002) Textural, chemical and isotopic insights into the nature and behaviour of metamorphic monazite. Chem Geol 191:183–207

Franke W (1989) Tectonostratigraphic units in the Variscan belt of central Europe. Geol Soc Am Spec 230:67–90

Franke W, Cocks LRM, Torsvik TH (2017) The Palaeozoic Variscan oceans revisited. Gondwana Res 48:257–284. https://doi.org/10.1016/j.gr.2017.03.005

Frassi C, Carosi R, Montomoli C, Law RD (2009) Kinematics and vorticity of flow associated with post-collisional oblique transpression in the Variscan Inner Zone of northern Sardinia (Italy). J Struct Geol 31:1458–1471

Fry N (1979) Random point distribution and strain measurement in rocks. Tectonophysics 60:89–105

Gerbault M, Schneider J, Corsini M, Reverso-Peila A (2018) Crustal exhumation during ongoing compression in the Variscan Maures–Tanneron Massif, France—Geological and thermomechanical aspects. Tectonophysics 746:439–458. https://doi.org/10.1016/j.tecto.2016.12.019

Genier F, Epard JL (2007) The Fry method applied to an augen orthogneiss: problemsand results. J Struct Geol 29:209–224

Giacomini F, Dallai L, Carminati E, Tiepolo M, Ghezzo C (2008) Exhumation of a Variscan orogenic complex: insights into the composite granulitic–amphibolitic metamorphic basement of south-east Corsica (France). J Metamorph Geol 26:403–436

Gillam BG, Little TA, Smith E, Toy VG (2013) Extensional shear band development on the outer margin of the Alpine mylonite zone, Tatare Stream, Southern Alps, New Zealand. J Struct Geol 54:1–20

Guillot S, Ménot RP (2009) Paleozoic evolution of the Extern Crystalline Massifs of the Western Alps. C R Geosci 341:253–265

Guerrera F, Martín-Martín M, Tramontana M (2019) Evolutionary geological models of the central-western peri-Mediterranean chains: a review. Int Geol Rev 1–22. https://doi.org/10.1080/00206814.2019.1706056

Hermann J, Rubatto D (2003) Relating zircon and monazite domains to garnet growth zones: age and duration of granulite facies metamorphism in the Val Malenco lower crust. J Metamorph Geol 21:833–852

Horstwood MSA, Foster GL, Parrish RR, Noble SR, Nowell GM (2003) Common-Pb corrected in-situ U-Pb accessory mineral geochronology by LA-MC-ICP-MS. J Anal At Spectrom 18(8):837–846. https://doi.org/10.1039/b304365g

Iaccarino S, Montomoli C, Carosi R, Montemagni C, Massonne HJ, Langone A, Jain AK, Visonà D (2017) Pressure–temperature–deformation–time constraints on the South Tibetan

detachment system in the Garhwal Himalaya (NW India). Tectonics 36:2281–2304
Iacopini D, Carosi R, Montomoli C, Passchier CW (2008) Strain analysis and vorticity of flow in the Northern Sardinian Variscan Belt: recognition of a partitioned oblique deformation event. Tectonophysics 221:345–359
Iacopini D, Frassi C, Carosi R, Montomoli C (2011) Biases in the three-dimensional vorticity analysis using porphyroclast system: limits and application to natural examples. Geol Soc Lond Spec Publ 360:301–318
Ildefonse B, Launeau P, Bouchez JL, Fernandez A (1992) Effect of mechanical interactions on the development of shape preferred orientations: a twodimensional experimental approach. J Struct Geol 14:73–83
Innocent C, Michard A, Guerrot C, Hamelin B (2003) U-Pb zircon age of 548 Ma for the leptynites (high-grade felsic rocks) of the central part of the Maures Massif. Geodynamic significance of the so-called leptyno-amphibolitic complexes of the Variscan belt of western Europe. Bull Soc Geol Fr 174:585–594
Jaffey AH, Flynn KF, Glendenin LE, Bentley CR, Essling AM (1971) Precision measurements of half-lives and specific activities of ^{235}U and ^{238}U. Phys Rev C 4:1889–1906. https://doi.org/10.1103/PhysRevC.4.1889
Jeffery G (1922) The motion of ellipsoidal particles immersed in a viscous fluid. Proc R Soc Lond A122:161–179
Kirscher U, Aubele K, Muttoni G, Ronchi A, Bachtadse V (2011) Paleomagnetism of Jurassic carbonate rocks from Sardinia: no indication of post-Jurassic internal block rotations. J Geophys Res 116:B12107
Kylander-Clark A, Hacker B, Cottle JM (2013) Laser ablation split-stream ICP petrochronology. Chem Geol 345:99–112. https://doi.org/10.1016/j.chemgeo.2013.02.019
Kurz GA, Northrup CJ (2008) Structural analysis of mylonitic fault rocks in the Cougar Creek Complex, Oregone Idaho using the porphyroclast hyperbolic distribution method, and potential use of SC0-type extensional shear bands as quantitative vorticity indicators. J Struct Geol 30:1005–1012
Law RD (2010) Moine Thrust zone mylonites at the Stack of Glencoul: II—results of vorticity analyses and their tectonic significance. Geol Soc Lond Spec Publ 335:579–602. https://doi.org/10.1144/SP335.24
Law RD (2014) Deformation thermometry based on quartz c-axis fabrics and recrystallization regimes: a review. J Struct Geol 33:129–161. https://doi.org/10.1016/j.jsg.2014.05.023
Law RD, Searle MP, Simpson RL (2004) Strain, deformation temperatures and vorticity of flow at the top of the greater Himalayan Slab, Everest Massif, Tibet. J Geol Soc Lond 161:305–320
Ludwig KR (2003) ISOPLOT 3.00: a geochronological toolkit for micrososft excel. Berkley Geocronology center, Berkely
Mammoliti E (2015) La "Ferriere–Mollières Shear Zone" (Massiccio dell'Argentera, Alpi Occidentali): rilevamento, analisi strutturale e cinematica del flusso nella zona di Ferriere (Argentera, CN). Unpublished Thesis, Università degli Studi di Pisa (Italy), pp 217
Matte P (1986) La Chaîne varisque parmi les chaînes paléozoïques péri-atlantiques, modèle d'évolution et position des grands blocs continentaux au PermoCarbonifère. Bull Soc Geol Fr 8:4–24
Matte P (2001) The Variscan collage and orogeny (480–290 Ma) and the tectonic definition of the Armorica microplate: a review. Terra Nova 13:117–121
McDonough WF, Sun SS (1995) The composition of the Earth. Chem Geol 120:223–253
McKinney ST, Cottle JM, Lederer GW (2015) Evaluating rare earth element (REE) mineralization mechanisms in Proterozoic gneiss, Music Valley, California. Geol Soc Am Bull 127:1135–1152
Montomoli C, Iaccarino S, Carosi R, Langone A, Visonà D (2013) Tectonometamorphic discontinuities within the Greater Himalayan Sequence in western Nepal (central Himalaya): insights on the nexhumation of crystalline rocks. Tectonophysics 608:1349–1370
Montomoli C, Iaccarino S, Simonetti M, Lezzerini M, Carosi R (2018) Structural setting, kinematics and metamorphism in a km-scale shear zone in the Inner Nappes of Sardinia (Italy). Ital J Geosci 137:294–310
Moussavou M (1998) Contribution à l'histoire thermo-tectonique varisque du massif des Maures par la typologie du zircon et la géochronologie U/Pb sur minéraux accessoires. PhD Thesis, University of Montpellier 2, France, pp 187
Morillon AC, Féraud G, Sosson M, Ruffet G, Crevola G, Lerouge G (2000) Diachronous cooling on both side of a major strike-slip fault in the Variscan Maures massif (SE France), as deduced from a detailed ^{40}Ar/^{39}Ar study. Tectonophysics 321:103–126
Mulchrone K (2007a) An analytical solution in 2D for the motion of rigid elliptical particles with a slipping interface under a general deformation. J Struct Geol 29:950–960
Mulchrone K (2007b) Shape fabrics in populations of rigid object in 2D: estimating finite strain and vorticity. J Struct Geol 29:1558–1570
Oliot E, Melleton J, Schneider J, Corsini M, Gardien V, Rolland Y (2015) Variscan crustal thickening in the Maures–Tanneron massif (South Variscan belt, France): new in situ monazite U-Th-Pb chemical dating of high-grade rocks. Bull Soc Geol Fr 186:145–169
Oncken O, von Winterfeld C, Dittmar U (1999) Accretion of a rifted passive margin: the Late Paleozoic Renohercynian fold and thrust belt (Middle European Variscides). Tectonics 18:75–91
Padovano M, Elter FM, Pandeli E, Franceschelli M (2011) The East Varisican Shear Zone: new insights into its role in the Late Carboniferous collision in southern Europe. Int Geol Rev 54:957–970
Padovano P, Dörr W, Elter FM, Gerdes A (2014) The East Variscan Shear Zone: geochronological constraints from the Capo Ferro area (NE Sardinia, Italy). Lithos 196–197:27–41
Passchier CW (1987) Stable position of rigid objects in non-coaxial flow: a study in vorticity analysis. J Struct Geol 9:679–690
Passchier CW, Trouw RAJ (2005) Microtectonics. Springer-Verlag, Berlin Heidelberg, p 101
Paton C, Woodhead JD, Hellstrom JC, Hergt JM, Greig A, Maas R (2010) Improved laser ablation U-Pb zircon geochronology through robust downhole fractionation correction. Geochem Geophys Geosyst 11(3):36. https://doi.org/10.1029/2009GC002618
Piazolo S, Passchier CW (2002) Control on lineation development in low to medium grade shear zones: a study from the Cap de Creus penisula, NE Spain. J Struct Geol 24:25–44
Platt PP, Vissers RLM (1980) Extensional structures in anisotropic rocks. J Struct Geol 2:397–410
Pyle JM, Spear FS (1999) Yttrium zoning in garnet: coupling of major and accessory phases during metamorphic reactions. Geol Mat Res 1:1–49
Pyle JM, Spear FS, Rudnick R, Mcdonough WF (2001) Monazite–xenotime–garnet equilibrium in metapelites and a new monazite–garnet thermometer. J Petrol 42:2083–2107
Ricci CA, Sabatini G (1978) Petrogenetic affinity and geodynamic significance of metabasic rocks from Sardinia, Corsica and Provence. Neues Jb Miner Mona 1:23–38
Rolland Y, Corsini M, Demoux A (2009) Metamorphic and structural evolution of the Maures–Tanneron massif (SE Variscan chain): evidence of doming along the transpressional margin. B Soc Geol Fr, special paper 180:217–230

Rollet N, Déverchère J, Beslier MO, Guennoc P, Réhault JP, Sosson M, Truffert C (2002) Back arc extension, tectonic inheritance, and volcanism in the Ligurian sea, western Mediterranean. Tectonics 21(3):6-1-23

Rosenbaum G, Lister GS, Duboz C (2002) Reconstruction of the tectonic evolution of the western Mediterranean since the Oligocene. In: Rosenbaum G, Lister GS (eds) Reconstruction of the Alpine-Himalayan Orogen. Journal of the Virtual Explorer, 8, 107–126

Rossi P, Durand-Delga M, Cocherie A (1993) Caractère volcanoplutonique du magmatisme calcoalcalin composite d'âgen Stéphanien supérieur Permien inférieur en Corse. C R Acad Sci, Paris Ser II 316:1779–1788

Rossi P, Oggiano G, Cocherie A (2009) A restored section of the "southern Variscan realm" across the Corsica–Sardinia microcontinent. C R Geosci 341(2–3):224–238

Rubatto D, Hermann J, Buick IS (2006) Temperature and bulk composition control on the growth of monazite and zircon during low-pressure anatexis (Mount Stafford, central Australia). J Petrol 47:1973–1996

Rubatto D, Chakraborty S, Dasgupta S (2013) Timescales of crustal melting in the Higher Himalayan Crystallines (Sikkim, Eastern Himalaya) inferred from trace element-constrained monazite and zircon chronology. Contrib Mineral Petr 165(2):349–372

Sanderson D, Marchini RD (1984) Transpression. J Struct Geol 6:449–458

Schneider J, Corsini M, Peila A, Lardeaux J (2014) Thermal and mechanical evolution of an orogenic wedge during Variscan collision: an example in the Maures–Tanneron Massif (SE France). J Geol Soc Lond 405:30–37

Scotese CR, McKerrow WS (1990) Revised World maps and introduction. Geol Soc Lond Mem 12:1–21. https://doi.org/10.1144/GSL.MEM.1990.012.01.01

Simonetti M (2015) La 'Ferriere - Mollieres Shear Zone' (Massiccio dell' Argentera, Alpi Occidentali): rilevamento geologico, analisi strutturale e cinematica del flusso nella zona del Vallone di Pontebernardo (Pietraporzio, CN). Unpublished Thesis, Università degli Studi di Torino (Italy), pp 182

Simonetti M, Carosi R, Montomoli C (2017) Variscan shear deformation in the Argentera Massif: a field guide to the excursion in the Pontebernardo Valley (CN, Italy). Atti Soc Tosc Sci Nat, Me Serie A 124:151–169. https://doi.org/10.2424/astsn.m.2017.25

Simonetti M, Carosi R, Montomoli C, Langone A, D'Addario E, Mammoliti E (2018) kinematic and geochronological constraints on shear deformation in the Ferriere–Mollières shear zone (Argentera–Mercantour Massif, Western Alps): implications for the evolution of the Southern European Variscan Belt. Int J Earth Sci 107(6):2163–2189. https://doi.org/10.1007/s00531-018-1593-y

Simonetti M, Carosi R, Montomoli C, Cottle JM, Law RD (2020) Transpressive deformation in the Southern European Variscan Belt: new insights from the Aiguilles Rouges Massif (Western Alps). Tectonics 39:e2020TC006153. https://doi.org/10.1029/2020TC006153

Simpson C, De Paor DG (1993) Strain and kinematic analysis in general shear zones. J Struct Geol 15:1–20

Stampfli GM, Borel GD (2002) A plate tectonic model for the Paleozoic and Mesozoic constrained by dynamic plate boundaries and restored synthetic oceanic isochrones. Earth Planet Sci 196:17–33

Stampfli GM, von Raumer LF, Borel GD (2002) Paleozoic evolution of pre-Variscan terranes: from Gondwana to the Variscan collision. Geol Soc Am 364:263–280

Stipp M, Stünitz H, Heilbron M, Schmid DW (2002) The eastern Tonale fault zone: a natural laboratory for crystal plastic deformation of quartz over a temperature range from 250° to 700°. J Struct Geol 24:1861–1884

Tollmann A (1982) Großräumiger variszischer Deckenbau im Moldanubikum und neue Gedanken zum Variszikum Europas. Geotektonische Forschungen 64:1–91

Tikoff B, Fossen H (1995) The limitation of three-dimensional kinematic vorticity analysis. J Struct Geol 17:1771–1784

Thompson AB, Schulmann K, Jezek J (1997) Thermal evolution and exhumation in obliquely convergent (transpressive) orogens. Tectonophysics 280:171–184

Turco E, Macchiavelli C, Mazzoli S, Schettino A, Pierantoni PP (2012) Kinematic evolution of Alpine Corsica in the framework of Mediterranean mountain belts. Tectonophysics 579:193–206

van Hinsbergen DJJ, Torsvik TH, Schmid SM, Maţenco LC, Maffione M, Vissers RLM, Gürer D, Spakman W (2020) Orogenic architecture of the Mediterranean region and kinematic reconstruction of its tectonic evolution since the Triassic. Gondwana Res 81:79–229. https://doi.org/10.1016/j.gr.2019.07.009

Vauchez A, Bufalo M (1985) La limite Maures occidentales–Maures orientales (Var, France) un décrochement ductile senestre majeur entre deux provinces structurales contrastées. C R Acad Sci Paris, Série II 301(14):1059–1062

Vauchez A, Bufalo M (1988) Charriage crustal, anatexie et décrochements ductiles dans les Maures orientales (Var, France) au cours de l'orogenèse varisque. Geol Runds 77(1):45–62

Vollmer FW (2015) EllipseFit 3.2 https://www.frederickvollmer.com/ellipsefit/. Accessed 15 Jan 2020

von Raumer JF, Bussy F, Schaltegger U, Schulz B, Stampfli GM (2013) Pre-Mesozoic Alpine basements—their place in the European Paleozoic framework. Geol Sci Am Bull 125:89–108

Wallis SR, Platt JP, Knott SD (1993) Recognition of synconvergence extension in accretionary wedges with examples from the Caiabrian Arc and the Eastern Alps. Am J Sci 293:463–495

Williams ML, Jercinovic MJ, Hetherington CJ (2007) Microprobe monazite geochronology: understanding geologic processes by integrating composition and chronology. Annu Rev Earth Planet Sci 35:137–175

Xypolias P (2010) Vorticity analysis in shear zones: a review of methods and applications. J Struct Geol 32:2072–2092